# *In-situ* and *ex-situ* catalytic upgrading of heavy crude oil

## Rational design and synthesis of nanocatalysts

by

# Kun Guo

University of
Stavanger

# Acknowledgements

First and foremost I want to express sincere gratitude to my supervisor Professor Zhixin Yu. It has been an honor to be his first Ph.D. student. I appreciate all his contributions to make my Ph.D. experience productive and fulfilling. I am also grateful to Professor Svein M. Skjæveland for his co-supervision.

Completion of my Ph.D. research would not have been possible without the help and support from many colleagues at University of Stavanger. Special thanks to Jostein Djuve, Jorunn H. Vrålstad, Inger Johanne M. Olsen, Per Eirik K. Widvey, Kim Andre N. Vorland, and Ola Ketil Siqveland for their support in laboratory work. Special mention also goes to Professor Vidar F. Hansen and Dr. Wakshum M. Tucho for TEM and SEM, and to Emanuela I. Kallesten and Caroline Ruud for XRD. The administrative support from both the Faculty and Department levels is deeply acknowledged.

Many Ph.D. candidates at the department have contributed extensively to both my personal and professional time in Stavanger. I am especially grateful to Dori Kalai and Kristian Stangeland for the nice interaction and collaboration at our Catalysis group. Great thanks are also extended to the Ph.D. coordinators and office mates for going beyond the call of duty. I am also thankful to the master and bachelor students for their assistance in the lab.

Special thanks to the National IOR Centre of Norway for the financial support of my Ph.D. project. It has been a great memory to be a member of the Centre. I also appreciate the financial support for a research exchange from Petroleum Research School of Norway.

I am also greatly appreciative for the impressive help from the external, particularly Professor Hailong Li at Mälardalen University, Professor Quan Shi at China University of Petroleum, Professors Yi Ding and Jun

iii

# Abstract

Rational design and synthesis of high-performance catalysts are of vital importance for the *in-situ* and *ex-situ* catalytic upgrading of heavy crude oil. Herein, we report the synthesis and application of monodispersed Ni and Co nanoparticles (NPs), common carbon materials, and carbon supported Ni as catalysts for the *in-situ* upgrading, together with thiospinel NPs and $MoS_2$-based monolayers as catalysts for the *ex-situ* upgrading.

Ni NPs with average sizes of 9 and 27 nm and Co NPs with an average size of 6 nm are prepared via the organometallic decomposition method by controlling the reaction temperature and surfactant amount. Catalytic performance of these NPs in the hydrodesulfurization (HDS) reaction is evaluated under reservoir-relevant conditions. The results show that the 9 nm Ni NPs exhibit the best HDS activity and stability compared to other catalysts, suggesting that the well-dispersed Ni NPs are promising candidates for the *in-situ* upgrading and recovery of heavy crude oil.

Similarly, carbon nanomaterials, including carbon nanotubes (CNTs), ketjenblack (KB) carbon, and graphene nanoplatelets (GNPs), are also studied as potential catalysts for the HDS of thiophene. Results show that key factors such as degree of graphitization and specific surface area play critical roles in the enhanced HDS activity of GNPs and KB compared with that of CNTs. This study opens new horizons in the implementation of carbon nanomaterials as sustainable metal-free catalysts for the *in-situ* upgrading and recovery of heavy crude oil.

Furthermore, Ni NPs supported on KB carbon, CNT, GNP, and zeolite are prepared and studied as catalysts in the upgrading of heavy crude oil (API 9.3° at 30 °C). Comparison of the activity of the pristine supports and supported catalysts indicates a possible synergistic effect between the Ni NPs and the support and Ni/KB performs as the best catalysts. The viscosity reduction and catalytic upgrading are further attributed to the

conversion of large molecule carboxylic acid compounds to derivatives with smaller carbon numbers and higher saturation. It is therefore concluded that the decomposition of carboxylic acid compounds contributes greatly to the viscosity reduction and Ni/KB can effectively catalyze the decomposition process.

First-row transition metal based thiospinels are prepared via a one-pot versatile strategy and for the first time investigated as HDS catalysts. Among the synthesized sulfides, $NiCo_2S_4$ presents the highest thiophene conversion, which is found to be correlated with the normal spinel structure with Ni cations located on the tetrahedral sites and Co cations on the octahedral sites. Study of the effect of synthetic temperature reveals that $NiCo_2S_4$ NPs prepared at higher temperatures exhibit higher structural stability and more surface sulfur vacancy. Our study suggests that the $NiCo_2S_4$ thiospinels with high activity and stability can represent a new promising class of industrial HDS catalysts.

Additionally, a one-step facile strategy is developed to prepare highly disordered ultrafine $MoS_2$ monolayers doped with Ni or Co via the thermal decomposition of organometallic precursors in the presence of elemental sulfur and oleylamine. Due to the abundant active edge sites enabled by the ultrafine monolayer structure, these sulfides exhibit significantly improved activity in the HDS and hydrodenitrogenation (HDN) reactions compared to the commercial multilayer $MoS_2$. It is proved that Co is better promoter than Ni for the HDS while the opposite for the HDN. Moreover, pyridine can be a competitive inhibitor for thiophene in binding to the active sites of the catalysts.

# List of Publications

I. *In-situ* heavy and extra-heavy oil recovery: A review.
   **K. Guo**, H. Li, and Z. Yu.
   *Fuel*, 2016, 185, 886–902.
   DOI: 10.1016/j.fuel.2016.08.047

II. Metallic nanoparticles for enhanced heavy oil recovery:
   promises and challenges.
   **K. Guo**, H. Li, and Z. Yu.
   *Energy Procedia*, 2015, 75, 2068–2073.
   DOI: 10.1016/j.egypro.2015.07.294

III. Monodispersed nickel and cobalt nanoparticles in
    desulfurization of thiophene for in-situ upgrading of heavy
    crude oil.
    **K. Guo**, V. F. Hansen, H. Li, and Z. Yu.
    *Fuel*, 2018, 211, 697–703.
    DOI: 10.1016/j.fuel.2017.09.097

IV. Carbon nanocatalysts for aquathermolysis of heavy crude oil:
    insights into thiophene hydrodesulfurization.
    **K. Guo**, M. Gu, and Z. Yu.
    *Energy Technology*, 2017, 5 (8), 1228–1234.
    DOI: 10.1002/ente.201600522

V. The effect of carbon supported nickel nanoparticles in the
   reduction of carboxylic acids for in-situ upgrading of heavy
   crude oil.
   **K. Guo**, Y. Zhang, Q. Shi, and Z. Yu.
   *Energy & Fuels*, 2017, 31 (6), 6045–6055.
   DOI: 10.1021/acs.energyfuels.7b00809

VI.      Nickel cobalt thiospinel nanoparticles as hydrodesulfurization catalysts: the importance of cation position, structural stability and sulfur vacancy.
**K. Guo**, Y. Ding, J. Luo, and Z. Yu.
Submitted.

VII.      One-step synthesis of ultrafine MoNiS and MoCoS monolayers as high-performance catalysts for hydrodesulfurization and hydrodenitrogenation.
**K. Guo**, Y. Ding, and Z. Yu.
Submitted.

*This thesis is based on the above seven papers.*

## Additional Publications

VIII.    **K. Guo**, H. Li, and Z. Yu. Size-dependent catalytic activity of monodispersed nickel nanoparticles for the hydrolytic dehydrogenation of ammonia borane. *ACS Applied Materials & Interfaces*, 2018, 10 (1), 517–525.

IX.    **K. Guo**, Y. Ding, J. Luo, and Z. Yu. NiCu bimetallic nanoparticles on silica support for catalytic hydrolysis of ammonia borane: composition-dependent activity and support size effect. *To be submitted*.

X.    **K. Guo**, M. Gu, and Z. Yu. Structure-dependent activity and selectivity of metal electrocatalysts towards carbon dioxide reduction. *In Preparation*.

## Conference Presentations and Proceedings

I.    **K. Guo** and Z. Yu. Size and support effects of monodispersed nickel nanoparticles on the catalytic hydrolysis of ammonia borane. *Oral* presentation at the Norwegian Catalysis Symposium 2017. Hurdal, Norway, 6–7 November, 2017.

II.    K. Guo, Y. Ding and **Z. Yu**. $H_2$ production from hydrolysis of ammonia borane: the effect of Ni particle size, support and alloying with Cu. *Oral* presentation at the 18th Chinese National Congress on Catalysis. Tianjin, China, 16–20 October, 2017.

III.    **K. Guo**, H. Li, and Z. Yu. Nanostructured metal electrocatalysts for carbon dioxide reduction with high activity and selectivity. *Poster* presentation at the 9th International Conference on Applied Energy. Cardiff, the United Kingdom, 21–24 August, 2017.

IV.   **K. Guo** and Z. Yu. Size-dependent catalytic dehydrogenation of ammonia borane over monodispersed nickel nanoparticles. *Oral* presentation at the International Conference on Energy, Ecology and Environment 2017. Stockholm, Sweden, 26–29 July, 2017.

V.    **K. Guo**, H. Li, and Z. Yu. Size-dependent catalytic dehydrogenation of ammonia borane over monodispersed nickel nanoparticles. *Proceedings* of the International Conference on Energy, Ecology and Environment 2017. Stockholm, Sweden, 26–29 July, 2017.

VI.   **K. Guo** and Z. Yu. Nickel decorated carbon nanocomposites as catalysts for the upgrading of heavy crude oil. *Proceedings* of the 19th European Symposium on Improved Oil Recovery (Th A02). Stavanger, Norway, 24–27 April, 2017.

VII.  **K. Guo**, Y. Zhang, Q. Shi, and Z. Yu. Carbon-supported nickel nanoparticles as catalysts for in-situ heavy crude oil recovery. *Oral* presentation at the 19th European Symposium on Improved Oil Recovery. Stavanger, Norway, 24–27 April, 2017.

VIII. **K. Guo**, V. F. Hansen, and Z. Yu. Synthesis and evaluation of monodispersed cobalt and nickel nanoparticles in the catalytic aquathermolysis of heavy crude oil. *Poster* presentation at the 16th International Congress on Catalysis. Beijing, China, 3–8 July, 2016.

IX.   **K. Guo**, P. Cuvillier, V. F. Hansen, and Z. Yu. Synthesis and evaluation of monodispersed cobalt nanoparticles in the catalytic aquathermolysis of heavy crude oil. *Poster* presentation at the IOR NORWAY 2016 Conference. Stavanger, Norway, 26–27 April, 2016.

# Table of Contents

xiii

# List of Figures

# List of Tables

# Abbreviations and Symbols

## Abbreviations

| | |
|---|---|
| BET | Brunauer–Emmett–Teller |
| BJH | Barrett–Joyner–Halenda |
| CNT | carbon nanotube |
| cP | centipoise |
| CSS | cyclic steam stimulation |
| DBE | rings plus double bond equivalence |
| EDX | energy dispersive X-ray |
| EOR | enhanced oil recovery |
| FT-ICR | Fourier transform ion cyclotron resonance |
| FTIR | Fourier transform infrared spectroscopy |
| GC | gas chromatography |
| GNP | graphene nanoplatelet |
| HCK | hydrocracking |
| HDM | hydrodemetallization |
| HDN | hydrodenitrogenation |
| HDO | hydrodeoxygenation |
| HDS | hydrodesulfurization |
| HT-SimDis | high-temperature simulated distillation |
| IFT | interfacial tension |
| ISC | *in-situ* combustion |
| JCPDS | Joint Committee on Powder Diffraction Standards |
| KB | ketjenblack |
| MS | mass spectrometry |
| NP | nanoparticle |
| PSD | particle size distribution |
| PV | pore volume |
| $PV_{meso}$ | mesopore volume |
| $PV_{micro}$ | micropore volume |
| $PV_{total}$ | total pore volume |
| SAGD | steam-assisted gravity drainage |
| SARA | saturate, aromatic, resin and asphaltene |
| SEM | scanning electron microscopy |
| SSA | specific surface area |

| TBP | true boiling point |
|-----|-------------------|
| TEM | transmission electron microscopy |
| TGA | Thermal gravimetric analysis |
| W/O | water/oil |
| XPS | X-ray photoelectron spectroscopy |
| XRD | X-ray diffraction |

## Symbols

| $\lambda$ | wavelength |
|-----------|-----------|
| $\Delta C$ | thiophene or pyridine conversion ratio |
| $C_0$ | initial concentration |
| $C_1$ | concentration after the reaction |
| $\Delta\eta$ | ratio of viscosity reduction |
| $\eta_0$ | initial viscosity |
| $\eta_1$ | viscosity after the reaction |

# 1   Introduction

The global oil demand projected by the Organization of the Petroleum Exporting Countries (OPEC) will reach 111.1 million barrels per day by 2040, with a 23.1% increment compared to current data.[1] Meanwhile, the consumption of conventional oils has resulted in declining reserves of such resources. As fossil fuel will remain to be the main energy source for the coming decades, there is a pressing need to exploit alternative fossil resources. Substantial efforts, therefore, have been devoted to the effective utilization of the unconventional heavy and extra-heavy (i.e., natural bitumen or oil sands) oils, which account for *ca.* 70% of total world oil reserves.[2-3]

## 1.1   Heavy oil

Heavy or extra-heavy oils are highly viscous oils that cannot easily flow at normal reservoir conditions. "Heavy" is defined because the density or specific gravity is higher than that of lighter oils (i.e., conventional oils). It is widely accepted to adopt specific gravity or viscosity to classify light, heavy and extra-heavy oils, as detailed in Table 1.1.[2,4-5] Specific gravity is measured based on the American Petroleum Institute in units named API degrees (°API); the lower the number of API degrees, the higher the specific gravity of the oil. Viscosity is measured in centipoises (cP) that represents the oil's resistance to flow; the higher the value, the higher the viscosity.

**Table 1.1** API gravity and viscosity of light, heavy and extra-heavy oils.

|                 | API gravity (°) | Viscosity (cP) | Density (kg/m³) |
|-----------------|-----------------|----------------|-----------------|
| Light oil       | > 22            | < 100          | < 934           |
| Heavy oil       | 10 ~ 22         | > 100          | 934 ~ 1,000     |
| Extra-heavy oil | < 10            | > 10,000       | > 1,000         |

1

Heavy oil and bitumen are mainly hydrocarbons with high molecular weights and high boiling points. Carbon atoms of most hydrocarbon molecules are above 60. These components can be categorized as saturate, aromatic, resin and asphaltene (SARA) based on the polarity and polarizability. Saturates comprise nonpolar fractions including linear, branched, and cyclic saturated hydrocarbons. Aromatics that contain one or more aromatic rings are relatively polarizable. The other two components, resin and asphaltene, are both polar substances. The major difference between them lies in that resins are miscible with *n*-heptane whereas asphaltenes are *n*-heptane insoluble and toluene soluble. Additionally, SARA also contain a considerable amount of nitrogen, oxygen, sulfur and metal elements, especially in the case of asphaltene, which is the main ingredient of heavy oil and bitumen. Geologically different reservoirs produce oils with different SARA proportion and sulfur content. For example, high sulfur heavy oils mostly exist in North America, South America and Middle East countries.[6]

## *1.2 Conventional recovery*

Traditionally, oil production is divided into three steps: primary, secondary and tertiary recoveries. In the production of heavy oils, primary and secondary recoveries are dominated by cold production and water flooding, as in the cases of Canadian oil sands, Venezuelan heavy oils and UK Continental Shelf. Cold production and surface mining are low-risk recovery approaches for heavy oils, but they are limited to the depth of reservoirs and relatively light crude inside.[7-8] Water flooding, as a popular secondary recovery method, is also not viable due to the huge viscosity difference between water and oils, leading to low sweep efficiency.[9] To achieve high recovery factors, enhanced oil recovery (EOR) is essential to follow. It is worth mentioning that oil viscosity is closely associated with temperature. Oil viscosity decreases with the increase of temperature. Accordingly, external thermal sources can be introduced to heat the oil and reduce the viscosity, which are generally

known as steam-based thermal injection. To improve the displacement efficiency, alternative recovery techniques using chemicals and gases have also been successfully implemented.

## 1.2.1 Thermal injection

Heavy oil recovery is problematic due to the inherent properties, such as high viscosity or even immobility, high C/H ratios and high heteroatom contents.[4-5] Complex formation configuration could also add additional difficulty in the oil production. Notwithstanding, the key mechanism for effective recovery has been identified to be the oil viscosity reduction and the resulting improved oil mobility. With this in mind, according to the temperature-viscosity correlation, various external energy sources are supplied to heat up the heavy oils, which eases their flow and extraction from the underground.

According to the different heat sources, architecture of injection and production wells, and the operating mechanism, a series of thermal injection methods have been developed, such as steam flooding, cyclic steam stimulation (CSS), *in-situ* combustion (ISC), and steam-assisted gravity drainage (SAGD).

## 1.2.2 Chemical injection

As mentioned above, water flooding is basically not applicable because the viscosity difference between heavy oil and water is too big, which results in a serious issue known as viscous fingering.[10] It depicts the situation that when a fluid displaces a more viscous one, the interface between them does not keep flat and perpendicular to the flow axis.[11] In case of water flooding, the less viscous water tends to bypass once it breaks through the viscous heavy oils because of the high interfacial tension (IFT) and immiscibility between the two phases. This fingering instability thus results in poor sweep and displacement efficiencies. In order to prevent this phenomenon, different chemicals are incorporated

to modify the properties of injected water. According to the chemical types, these methods are generally categorized as surfactant flooding, polymer flooding, alkaline flooding and solvent flooding.[12-14] It should be emphasized that chemical injection is mostly used for heavy oil EOR but not very suitable for immobile bitumen or oil sands. In addition, instead of reducing the oil viscosity, which is the main mechanism of the thermal methods, lowering the IFT, mobility control and wettability alteration are the alternative solutions to improve the mobility of viscous oils in all chemical-based recovery technologies.[15-18] In particular, when immiscible water and oil are in contact, an interface will form between the two phases accompanied with considerable IFT. The high IFT is accountable for the resistance of flow of residual oils. IFT reduction is thus a key factor in the mobility improvement of heavy oils.

### 1.2.3 Gas injection

Gas injection is one of the oldest EOR techniques used for conventional oils, and can also be applied for the recovery of heavy oils. Typically, a readily available gas, like natural gas, $CO_2$, $N_2$ or flue gas that exhibits certain miscibility with oil in a compressed form, is injected into the reservoir to maintain the pressure, under which gas saturation at the interface zone increases. This high gas saturation can generate significant oil swelling, reduce the IFT between two interacting fluids and thus improve the oil displacement efficiency. However, issues related to gas segregation, viscous fingering or channeling, mobility control remain problematic for the gas flooding techniques.

## 1.3    Upgrading in the refinery

Crude oil must be upgraded in the oil refinery to produce transportation fuel products. After the preliminary distillation, a series of hydrotreating processes, including the hydrocracking (HCK), hydrodesulfurization (HDS), hydrodenitrogenation (HDN), hydrodenitrogenation (HDO), and hydrodemetallization (HDM) reactions, are applied and all of them are

catalytic processes. In fact, catalytic processes are the pillars of oil refining.

Hydrotreating of the crude oil can be dated back to the World War II, when the sulfur and nitrogen in the oil were removed by the HDS and HDN processes. Since then, decades of efforts devoted by chemists and engineers have identified the sulfided molybdenum (Mo) or tungsten (W) promoted by nickel (Ni) or cobalt (Co) and supported on $\gamma$-$Al_2O_3$ as the most prevailing catalysts in the oil refineries.

# 2 Literature Review

## *2.1 In-situ catalytic upgrading*

This chapter is based on the review Paper I and II.[19-20]

Undoubtedly, viscosity reduction is the key to the success of *in-situ* recovery of heavy and extra-heavy oils. Conventional thermal injection methods have proved that heat-induced mechanism is effective to improve mobility. However, inherent economic and environment concerns related to such processes are driving people in both academia and industry to search alternative solutions. *In-situ* upgrading by nanocatalysis is one potential technology that could bring a cost-efficient process with high recovery factor. More specifically, *in-situ* catalysis allows the upgrading and recovery to occur simultaneously. With the catalytic decomposition of long chain hydrocarbons, lighter fractions with smaller molecular weight are formed, which implies viscosity reduction and mobility improvement of the resulting heavy oils. Despite emerging as a new technology, this concept is receiving extensive investigation nowadays.

### *2.1.1 Catalysts for in-situ upgrading*

In the 1980s, Hyne *et al.*[21] discovered that steam injection brought not only the physical reduction of heavy oil viscosity by temperature increase, but also the chemical reactions with some oil components, leading to beneficial changes of the oil property and composition. This reaction route was named as "aquathermolysis" by these researchers. However, their further studies revealed that the chemical changes are reversible because heteroatoms (S, N, and O) interact with other molecules by van der Waals forces, leading to polymerization and thus the regression of high viscosity.

Inspired by the aquathermolysis, researchers have moved forward by introducing catalytic reaction into the reservoir. Proper catalysts can facilitate the chemical reactions of heavy feeds to a large extent, leading to effective and irreversible viscosity reduction. This *in-situ* catalysis thereby enables the realization of underground upgrading and enhanced recovery. To this end, ongoing studies are being focused on the exploration of active, stable and reliable catalysts at laboratory and field scales. Generally, reported catalysts for enhanced recovery of heavy oil and bitumen can be roughly classified as (1) water-soluble catalysts, (2) oil-soluble catalysts, (3) amphiphilic catalysts, (4) minerals, zeolites, and solid superacids, and (5) metallic nanoparticles (NPs).

### 2.1.1.1    Water-soluble catalysts

For water-soluble, oil-soluble and amphiphilic catalysts, they have the advantage of ensuring sufficient contact between the active species and reactants. Hyne *et al.*[21] and Rivas *et al.*[22] observed that the Ni(II) and Co(II) salts had an impact on the aquathermolysis. Later on, Clark *et al.*[23-25] further confirmed this effect by systematically studying a series of Al(III), first row transition metal Sr(III), VO(II), Cr(III), Ni(II) and Cu(II), and Group VIIIB metal Fe(II), Co(II), Ni(II), Rh(III), Os(III), Ir(III), Ru(III), Pt(II) and Pt(IV) salts. They concluded that Al(III) and first row metal species were very reactive in the aquathermolysis of thiophene and tetrahydrothiophene, two typical model compounds for organosulfur molecular types in heavy oils. Besides, Pt(IV) is the most active metal in Group VIIIB to reduce sulfur content, with 40% and 56% sulfur reduction for the thiophene and tetrahydrothiophene, respectively. Moreover, Chen's group[26] found that different metal ions had distinctive roles in catalyzing the aquathermolysis reactions by studying the $Fe^{3+}$ and $Cu^{2+}$ ions.

### 2.1.1.2    Oil-soluble catalysts

The limitation that water-soluble catalysts cannot effectively mix with the oil phases inspires the development of oil-soluble catalysts. Wen *et al.*[27] synthesized molybdenum oleate as an oil soluble catalyst and experimental results showed that with 0.5 wt. % catalyst the viscosity reduction of heavy oils could be up to 90%. Furthermore, this catalyst was proved effective to reduce the viscosity at field tests at Liaohe oilfield in China. Zhao *et al.*[28] studied Ni(II) and Co(II) oleate in the presence of petroleum sulfonate as an emulsifier and toluene as a hydrogen donor. They demonstrated that the thermal stability and durability of this catalyst as well as its effectiveness in viscosity reduction were better than that of water-soluble catalysts. Impressively, with a low content of 0.4 wt. %, the catalyst reduced the viscosity by 90% at 180 °C and sulfur content decreased by 87.5%. Besides, Ni(II) and Fe(II) naphthenate[29-30], organic Ni(II) and Co(II) salts[31-34] and Fe(III) tris(acetylacetonate)[35] catalysts with various hydrogen donors of tetralin, formamide, and formic acid have also achieved remarkable performance in the reduction of heavy oil viscosity. Therefore, it is commonly accepted that oil-soluble catalysts show better catalytic activity than that of water-soluble catalysts.[29]

### 2.1.1.3    Amphiphilic catalysts

Even though oil-soluble catalysts have shown prominent activity through better contact, they still suffer from the problem of catalyst separation from the oil phase, resulting in insufficient utilization of the catalytically active metal species. Therefore, amphiphilic catalysts that combine the benefits of water-soluble and oil-soluble ones are proposed. Chen's group[36] designed aromatic sulfonic iron composed of an active metal cation and an amphiphilic anion. This amphiphilic anion improved the dispersion of cations into the oil and helped the catalyst remain stable at the water-oil interface. Accordingly, an apparent viscosity reduction of 90.7% at 200 °C was realized; field tests also achieved eminent

enhancement with stable viscosity reduction of up to 82.3%. This group[37] also synthesized a new type of Gemini catalyst with transition metal as the active center and Gemini surfactant as the ligand. Over 90% viscosity reduction at both laboratory and field scale tests was achieved at a relatively low temperature of 170 °C. An interesting study was performed by Chao *et al.*[38] by combining hydrogen precursor and active species. The authors utilized alkyl ester sulfonate copper as a bifunctional catalyst and observed 90.7% viscosity reduction after 24 h using 0.3 wt. % catalyst at 240 °C. They claimed that this eco-friendly catalyst could be prospective for field applications. Additionally, several chelates[39-43] and metal dodecylbenzenesulfonates[44-45] are also reported with superior performance. However, the temperature-dependent activity needs further validation taking into consideration that the temperature in the reservoirs will normally be lower.

### 2.1.1.4    Minerals, zeolites, and solid superacids

Another important type of catalysts are the heterogeneous ones including minerals, zeolites, and solid superacids. Mineral is an ideal catalyst due to its natural abundance in the reservoir. This concept was first testified by Monin *et al.*[46] who found that seven different types of minerals all behaved similarly by promoting the cracking reactions of heavy crude oils. Fan *et al.*[47-48] and Ovalles *et al.*[49] also observed a synergetic effect of minerals and steam on the aquathermolysis of heavy oils. Natural zeolites are economic and abundant minerals. When activated properly to possess certain acidity, they also showed considerable activity in heavy oil viscosity reduction.[50-53] Solid superacids with strong acidity have also been employed as catalysts. Strausz *et al.*[54] reported that tetrafluoroboric acid (HF·$BF_3$) as an active catalyst led the reactions to proceed by depolymerization and hydrogenation with the main products of volatile organic compounds and alkylbenzenes. Results from this study triggered the investigation of other heteropoly acids and modified zirconia as alternatives since the water solubility of HF·$BF_3$ poses recovery problems. Both nano-keggin $K_3PMo_{12}O_{40}$ and $H_3PMo_{12}O_{40}$

were found to give apparent large viscosity reduction due to their unique properties in acidity, redox and pseudo-liquid phase reactions.[55-56] In addition, zirconia activated by sulfate groups or metal oxides are also widely used superacids. Li's group[57] demonstrated that $SO_4^{2-}/ZrO_2$ superacid doped with $Ni^{2+}$ or $Sn^{2+}$ catalyzed the visbreaking of Shengli heavy oils. The content of resin, asphaltene, sulfur and nitrogen decreased significantly.

Although the reported catalysts have displayed satisfactory activities in the upgrading of heavy oil and bitumen, issues regarding catalyst recycling, deactivation and applicability are still troublesome for commercial implementation. Specifically, water-soluble catalysts face shortcomings of the inadequate contact between catalysts and the oil phase, whereas oil-soluble catalysts pose the problem of catalyst separation. The catalytic activity of most minerals is insufficient, or even negligible, and the injection of mineral particles is practically difficult. In addition, high activities of solid acids at low reservoir temperatures are problematic. To operate at relatively mild conditions, it is imperative to continue looking for highly active and durable catalysts. Among the reported catalysts, nanomaterials have gained growing attention recently. Owing to the unique properties of the nanoscale materials, such as high inherent catalytic activity, high surface area to volume ratio, efficient transport inside porous rocks, and controllable synthesis for specific functionalities, nanocatalysts are being developed to catalyze the *in-situ* chemical reactions in reservoirs, in which heavy oil and bitumen are converted to lighter products that meet pipeline and refinery specifications.

### 2.1.1.5 Metallic NPs

Metallic NPs have long been used in the upgrading of heavy oil and bitumen in petroleum refineries, but not in the subsurface reservoirs. Various transition metals and oxides such as $Mo$[58-59], $Fe$[60-62], $Ni$[63-68], $Cu$[69-70], $Fe_2O_3$[71-74], $CuO$[61,75] and alloys[76-81] based catalysts have been

reported. For example, Li *et al.*[63] prepared nano-Ni microemulsion and applied them in the aquathermolysis of extra-heavy oil. The study demonstrated that the nano-Ni could catalyze the visbreaking, sulfur removal and asphaltene conversion. The synergetic effects of upgrading, emulsification and diluting resulted in a high viscosity reduction of 98.9%. Hashemi *et al.*[78-80] also reported microemulsions containing trimetallic (W, Ni, and Mo) colloidal NPs as aquathermolysis catalysts and their injectivity in a packed bed reactor along with enhanced bitumen recovery was demonstrated. To clarify the underlying mechanism, Babadagli's[61] and Ovalles's[74] groups explored the influence of metal type, size and concentration of NP on the catalytic activity. They both recognized that these parameters were very important and should be optimized to achieve better overall performance. The high thermal conductivity of metallic NPs can also improve the energy efficiency. Accordingly, it is proposed that metallic NP assisted *in-situ* heavy oil recovery is a new and promising alternative to supplement conventional thermal methods although substantial research and development are needed for commercial field application.

## 2.1.2 Upgrading mechanism

The viscosity reduction of heavy oils relies on two pathways, by virtue of either redistributing internal hydrogen atoms or introducing external hydrogen donors. For the former, hydrogen is migrated from one part of heavy hydrocarbons to the others, which means upgrading would occur together with potential formation of detrimental coke. It is therefore favorable to introduce external hydrogen sources, such as water, tetralin and $CH_4$, to avoid coke formation. However, the hydrotreating processes are kinetically sluggish and active catalysts needs to be applied. The incorporation of catalysts can facilitate the hydrotreating reactions to proceed at mild conditions and eventually turn the reservoirs into subsurface reactors.

As mentioned previously, heavy oil and bitumen are heavy hydrocarbons featured with high C/H ratios and considerable amounts of N, S, O and metal elements. When steam is injected, heat energy is supplied to break large molecules into smaller and lighter ones. Hyne *et al.*[21] proposed the following reaction mechanism in aquathermolysis:

$$RCH_2CH_2SCH_3 + 2H_2O = RCH_3 + CO_2 + H_2 + H_2S + CH_4$$

The cleavage of C–S bond brings not only reduced molecular size and sulfur removal but also gaseous products. Interestingly, the comparative analysis of Canadian and Venezuelan heavy crude oils reveals that sulfur content is the key factor in aquathermolysis and the viscosity reduction is largely dictated by the C–S bond breakage. However, aquathermolysis of the Liaohe heavy crude oil with low sulfur content (< 0.5%) in Northeast China has also been reported. This controversial mechanism indicates the complexity of the chemical reactions involved in the aquathermolysis process.[38,41-43]

HCK entails the theoretical feasibility for this "underground refinery". Nonetheless, it is only thermodynamic favorable at high temperatures. An active catalyst needs to be introduced to lower the activation energy barrier. Catalytic HCK will be a two-stage process combining cracking and hydrogenation processes promoted by catalysts. Cleavage of C–C and C–R (R = S, N, and O) bonds induced by the coordination effect of transition metal atoms is the main route for the exposed intermediate carbon radicals to adsorb free hydrogen atoms. Among all the chemical bonds existing in hydrocarbon molecules, C–S bond is found to be the most catalytically active.[82] Furthermore, several studies have shown that heteroatom (N, O and S) containing groups in the heavy oil could cause polymerization with the formation of hydrogen bonds, adversely leading to the viscosity regression. *In-situ* sulfur removal could also alleviate the burden of the desulfurization process in refineries. Accordingly, the HDS, HDN, HDO and HDM reactions, in particular the HDS, play an important role to upgrading heavy oils with high quality.

The introduction of catalysts also provides additional reaction pathways for the viscosity reduction. Isomerization, ring opening, oxygenation, alcoholization, esterification, and reconstruction reactions are observed when using $Fe^{3+}$ and $Mo^{6+}$ as catalytic ions.[39] Wang's group[83] suggested that with the aid of superacid $WO_3/ZrO_2$, the presence of water was not required. Galarraga et al.[76] reported that NiWMo submicronic catalysts reduced both the viscosity and microcarbon residue. Impressively, Shokrlu et al.[61] observed a viscosity reduction once the metal NPs were mixed with oil samples at low temperatures owing to the exothermic chemical reactions. This result underlines the potential of utilizing highly active NPs as *in-situ* catalysts in heavy oil upgrading and recovery. They have further suggested the beneficial effect of high thermal conductivity of metals since efficient heat transfer is crucial in the thermal recovery methods. Most of the current studies are limited to the simulated reservoir conditions in laboratory, the multiple beneficial functions of metallic NPs entitle this promising technology to be further investigated and developed.

## *2.1.3 Catalyst design and synthesis*

Synthesis of metallic nanomaterials is enriched along with the fast advancement of nanotechnology in multidisciplinary applications and is already a well-established field. Precise manipulation of the size, shape, composition, type, and surface functionality has all been possible by the selective control of synthesis parameters. Synthetic approaches can be generally divided into the top-down and bottom-up methods. It is widely accepted that the chemical methods are very suitable for the controlled synthesis of multifunctional nanomaterials.

Among different chemical synthetic approaches, the microemulsion method is widely used for the preparation of metallic NPs in heavy oil phase. Typically, a W/O microemulsion is prepared by mixing water, oil (*e.g.*, vacuum gas oil) and an emulsifying agent (*e.g.*, surfactants). A solution containing corresponding salt precursors is then added and

blended uniformly with the W/O emulsion. Subsequently, another solution, precipitation agent or reduction agent, is added to activate the nucleation and growth of NPs, which exist inside individual water droplets that are covered by emulsifier and suspended steadily in the oil phase. Besides, surface-modified silica can also be introduced to support the dispersed NPs with the formation of stable suspension.[62,74,81]

Structure–activity relationship remains state-of-the-art in the functional design and synthesis of NPs. The effect of metal type, size, shape, composition, dispersity, concentration and support on the activity should be elucidated to maximize the catalytic activity, which could further enable the NP-assisted recovery method be adapted to the harsh reservoir conditions.

Among the transition metals, Ni is regarded as the most promising one because of its high activity and low cost. Shokrlu *et al.*[61] studied Fe, Cu, Ni, $Fe_2O_3$ and CuO NPs with different nano- and micron- sizes as viscosity reducers and identified the optimal variables such as metal type, size and concentration. They concluded that optimal concentration of NPs is strongly dependent on the heavy oil composition, especially the asphaltene content. Proper selection of metal type and size should also be based on the composition analysis. Wang *et al.*[83] declared that diffusion of $WO_3$ onto $ZrO_2$ was improved by hydrothermal method. The well-dispersed $WO_3/ZrO_2$ offered additional activity enhancement. In addition, the importance of catalyst composition and synergetic effect of metal alloying is reported by Nassar's group.[79-80] They assembled trimetallic (W–Mo–Ni) NPs with a specific metal ratio and stated that Mo was used as a hydrogenolysis metal, while W was inserted to improve the hydrogenation activity of the trimetallic catalyst and Ni acted as a promoter. It is noteworthy that exposed facet of NPs is also a factor that deserves further study because it is well know that different crystal planes exhibit different catalytic activities.

## *2.2 Ex-situ catalytic upgrading*

*Ex-situ* upgrading of heavy crude oil refers to the hydrotreating processes in the oil refineries, particularly the HDS and HDN. Emission of sulfur dioxide ($SO_2$) and nitrogen oxides ($NO_x$), due to the combustion of petroleum-derived fuels such as gasoline and diesel, has been identified as a major cause of the notorious acid rain and air pollution. To protect the environment, many countries have issued increasingly stringent legislations to reduce the contents of sulfur and nitrogen in transportation fuels to an ultralow level. Such measures are thus applying high pressure to the oil refineries. Either the severity of the reaction conditions or the improvement of employed catalysts should be considered for producing ultraclean fuels with S and N contents meeting the standards.

Mo(W) sulfides promoted by Co(Ni) and supported on $\gamma$-$Al_2O_3$ have been used as the industrial HDS and HDN catalysts for decades. It is well documented that the active species in the catalysts consist of Mo(W), Co(Ni) and S atoms on the edges of the lamellar Mo(W) sulfides. The Mo(W)Co(Ni)S are prepared by the two-step precipitation and post-sulfidation, which usually generate catalysts with low density of active sites and unfavorable nanostructure. Besides, the sulfidation process is often inadequate, resulting in a co-existence of oxides and sulfides in the catalysts. This two-step synthetic method makes it challenging to tailor-make and fine-tune the resulting catalyst structure. To improve the classic Mo(W)Co(Ni)S catalysts, two research directions have been proposed, either by exploring new potential catalyst systems or by improving the design and synthesis to create high density and availability of the active sites of the Mo(W)Co(Ni)S catalysts. For instance, Lai *et al.*[84] reported the one-step synthesis of a NiMoS flower structure composed of sulfide nanosheets, which exhibited excellent activities in the HDS of thiophene and 4,6-dimethyldibenzothiophene due to the high density of active sites in this flower structure. Tang *et al.*[85] reported that by introducing Mo and Co species into the meso- and micropores of

mordenite nanofibers, a much higher activity and longer catalyst life in the HDS of 4,6-dimethyldibenzothiophene were achieved by the CoMo/mordenite compared with a conventional CoMo/$\gamma$-Al$_2$O$_3$ catalyst.

Lately, transition metal sulfides with spinel-type AB$_2$S$_4$ structure (i.e., thiospinel, A, B = Ni, Co, Fe, Cu, *etc.*) emerge as an important material for diverse applications such as catalysis, energy harvesting, storage and conversion, and electronics.[86] In an AB$_2$S$_4$ unit cell, as illustrated in Figure 2.1, metal A and B atoms occupy the tetrahedral and octahedral sites, respectively, and their positions can shift within the cell, leading to the normal and inverse spinel structures. The multivalence nature of both A and B metals endows the thiospinel-based materials with unique redox properties, good electrical conductivity and surface-abundant sulfur vacancies.[87-89] These superiorities enable the thiospinels to be high performance catalysts in many chemical reactions.[86] Nevertheless, the application of thiospinels as catalysts for the HDS remains unexplored, particularly the NiCo$_2$S$_4$ and CoNi$_2$S$_4$ since Ni and Co sulfides are well-established active species for the HDS. Potential advantages of thiospinels as HDS catalysts can originate from (1) the unique combination of different metal sulfides with multivalence into single-phase sulfide with stoichiometric composition and ordered atomic arrangement, (2) the abundant sulfur vacancies at the thiospinel surface that could serve as reactive sites for sulfur abstraction, (3) the direct utilization of thiospinels to avoid the troublesome sulfidation step, (4) the feasibility of tailor-making rational structure of thiospinel catalysts, and (5) the low cost, high abundance, low toxicity and good flexibility of thiospinels fabricated with first-row transition metals. It is thus of great interest to investigate the potential application of thiospinel-based catalysts for the industrially important HDS reaction.
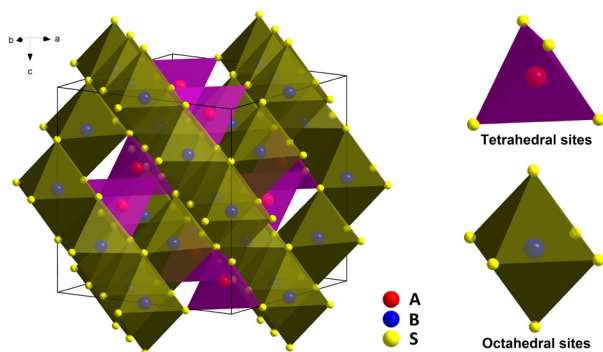
**Figure 2.1** Illustration of the spinel-type crystal structure of $AB_2S_4$ (A, B=Ni, Co, Fe, Cu, etc.). Metal A cations occupy the tetrahedral sites and Metal B cations occupy the octahedral sites.

Alternatively, one-step synthetic strategy, using either the decomposition of thiosalts or the direct sulfidation of metal precursors, has been adopted to prepare the layered Mo-based materials not only as catalysts for HDS and HDN but also as key materials in distinct applications. Yan *et al.*[90] obtained ultrathin $MoS_2$ nanoplates with rich active sites by the direct solvothermal decomposition of $(NH_4)_2MoS_4$. Afanasiev *et al.*[91] prepared highly dispersed $MoS_2$ by reducing $(NH_4)_2MoS_4$ in the presence of a surfactant. Direct sulfidation of ammonium molybdate with elemental S was reported to synthesize $MoS_2$ nanoflowers constructed by single-layered or few-layered $MoS_2$ nanosheets.[92-93] By one-pot reaction of $Mo(CO)_6$ and S in xylene solvent, Cho's group[94] prepared $MoS_2$ nanoplates that consist of disordered graphene-like sheets. It has also been proved that Co(Ni) precursors can be readily introduced in the synthesis to get $MoS_2$ promoted with Co(Ni).[84,95] These studies have demonstrated that the one-step methods offer high feasibility to tailor-make and fine-tune the nanostructure and morphology of Mo sulfides. Furthermore, the resulting sulfides by one-step synthesis normally end up being unsupported, which endows them with abundant and stable active sites. The unsupported Mo(W)Co(Ni)S catalysts have also been testified to perform better in the HDS and HDN compared to the traditional supported ones.[96-99] Therefore, one-step synthesis of unsupported Mo(W)Co(Ni)S catalysts with well-designed structure

holds great potential for realizing high catalytic performance in the HDS and HDN.

The catalytic properties of $MoS_2$ change dramatically when the stacking layers are exfoliated into monolayers, which is analogous to graphene and graphite. Distorted $MoS_2$ monolayers often contain a high density of dislocations, which creates abundant defect sites that are catalytically active. In addition, the reduction of the lateral size of $MoS_2$ monolayers to nanoscale can turn the inactive basal plane sites into active edge sites. Nevertheless, the facile preparation of $MoS_2$ monolayers with ultrafine lateral sizes remains challenging and further efforts are required.

# 3  Objectives and Scope of the Study

Driven by the pressing need for effective recovery and upgrading of heavy crude oil and the increasingly stringent environmental legislations for sulfur and nitrogen emission, tremendous efforts have been made in the research of *in-situ* and *ex-situ* catalytic upgrading of heavy crude oil. This thesis is a continuation of such efforts with an emphasis on the rational design and synthesis of novel nanocatalysts. The first part of this thesis focuses on the development of metal NPs, carbon materials and carbon supported NPs as catalysts for *in-situ* upgrading, while the second part of this thesis aims at the study of thiospinel NPs and improved MoNiS and MoCoS catalysts for *ex-situ* upgrading. Specific objectives of the papers are formulated as below.

In Paper III[100], we explore two types of metal NPs (Ni and Co) as catalysts in the HDS reaction using thiophene as a sulfur-containing model compound. Ni and Co NPs are in house prepared via the thermal decomposition method. These NPs together with the commercial Ni and Co particles are studied to investigate the size-dependent activity of metallic catalysts. In addition, ratio between thiophene and hydrogen donor, catalyst dosage, temperature, and reaction duration are optimized. To understand the catalytic behavior of NPs, the morphology and size of NP catalysts after the HDS reaction are also characterized.

Paper IV[101] concerns the study of HDS reaction by employing several widely used carbon materials as metal-free catalysts, including CNTs, ketjenblack (KB) carbon, and graphene nanoplatelets (GNPs), at reservoir-relevant conditions of temperatures of 120–180 °C and pressures of <3 MPa. Parameters such as catalyst dosage, temperature, and reaction time are investigated to improve the catalytic performance. The results presented herein contribute to the future advancement of metal-free, carbon-based nanocatalysts in the implementation of *in-situ* upgrading and recovery of heavy crude oil.

Based on Paper III and IV, Paper V[102] further addresses the application of carbon supported Ni catalysts for the upgrading of heavy crude oil. KB carbon, GNPs, CNTs, and zeolite supported Ni NPs are prepared and employed as catalysts. The potential synergistic effect of the support and Ni NPs is explored in the upgrading of heavy crude oil. Upgrading of heavy crude oil (API 9.3° at 30 °C) are conducted in a batch reactor under different reaction conditions to investigate the effect of temperature, reaction time, and hydrogen donor on the catalytic performance. The upgrading activities of the pristine supports and supported catalysts are also comparatively investigated. Advanced oil sample analysis before and after the upgrading reactions allows the understanding of underlying reaction mechanism.

In Paper VI, we propose for the first time the application of thiospinel NPs as a new class of HDS catalysts. Facile, one-pot synthesis of a series of earth-abundant transition metal-based monosulfide and thiospinel NPs is prepared by reducing the metal acetylacetonate precursors with elemental sulfur in the presence of oleyamine. The versatility of this synthetic approach is validated with the successful synthesis and detailed characterization of sulfides including NiS, $Co_3S_4$, $NiCo_2S_4$, $CoNi_2S_4$, $NiFe_2S_4$ and $CuCo_2S_4$. These sulfides are evaluated with respect to their catalytic activities in the HDS of thiophene using a batch reactor. The synergistic effect between Ni and Co atoms together with their specific site occupancy in the thiospinel structure is verified. As $NiCo_2S_4$ NPs present the highest HDS activity but insufficient stability, we further synthesize $NiCo_2S_4$ NPs at six different temperatures to study the effect of synthetic temperature on the HDS activity of $NiCo_2S_4$ NPs. It is revealed that the structural stability of $NiCo_2S_4$ thiospinels is important for achieving high HDS activity. Reusability of the optimized $NiCo_2S_4$ catalyst is also examined for potential industrial applications.

In Paper VII, a one-step, facile synthetic method based on the thermal decomposition of organometallic precursors and sulfidation with sulfur in oleyamine is developed to prepare highly dispersed, unsupported

MoS$_2$ monolayers doped with Ni or Co (designated as MoNiS and MoCoS). Detailed characterization techniques are utilized to acquire compositional and structural information of the obtained MoS$_2$, MoNiS and MoCoS. Their catalytic performance in both individual and simultaneous HDS and HDN is studied using a batch reactor with thiophene and pyridine as the S- and N-containing model compounds, respectively. Difference of the Co and Ni as promoting cations in HDS and HDN is examined. The competing adsorption of thiophene and pyridine to the active sites is evidenced when comparing the results from simultaneous HDS and HDN with the individual reaction. The reusability of MoNiS and MoCoS catalysts is also tested in consecutive reactions. This study highlights the importance of advanced synthetic strategy for enhancing the performance of nanostructured Mo-based sulfides as industrial HDS and HDN catalysts.

# 4 Experimental

## 4.1 Materials and chemicals

All the materials and chemicals used in this thesis are used as received without further treatment. Information of the chemicals is listed in Table 4.1.

Table 4.1 Information of the used chemicals.

| Chemical | Abbreviation | Purity and Supplier |
|---|---|---|
| nickel(II) acetylacetonate | $Ni(acac)_2$ | 95%, Sigma-Aldrich |
| cobalt(III) acetylacetonate | $Co(acac)_3$ | 98%, Sigma-Aldrich |
| dicobalt octacarbonyl | $Co_2(CO)_8$ | ≥90%, Sigma-Aldrich |
| iron(III) acetylacetonate | $Fe(acac)_3$ | ≥99.9%, Sigma-Aldrich |
| copper(II) acetylacetonate | $Cu(acac)_2$ | ≥99.9%, Sigma-Aldrich |
| molybdenum hexacarbonyl | $Mo(CO)_6$ | ≥99.9%, Sigma-Aldrich |
| oleylamine | OAm | 70%, Sigma-Aldrich |
| trioctylphosphine | TOP | 97%, Sigma-Aldrich |
| 1,2-dichlorobenzene | DCB | 99%, Sigma-Aldrich |
| oleic acid | OA | ≥99%, Sigma-Aldrich |
| trioctylphosphine oxide | TOPO | 99%, Sigma-Aldrich |
| 1,2,3,4-tetrahydronaphthalene | tetralin | 99%, Sigma-Aldrich |
| sulfur | S | 99.998%, Sigma-Aldrich |
| ethylene glycol | EG | 99.8%, Sigma-Aldrich |
| sodium borohydride | $NaBH_4$ | ≥98.0%, Sigma-Aldrich |
| nickel(II) nitrate hexahydrate | $Ni(NO_3)_2 \cdot 6H_2O$ | ≥98.5%, Sigma-Aldrich |
| carbon nanotube | CNT | Shenzhen Nanotech Port |
| Ketjenblack EC-600 JD | KB | AkzoNobel |
| graphene nanoplatelet | GNP | American Elements |
| zeolite, Si:Al = 5.1:1 | | Alfa Aesar |
| molybdenum disulfide | $MoS_2$ | 99%, nanopowder, Sigma-Aldrich |

## 4.2 Catalyst preparation

### 4.2.1 Synthesis of Ni and Co NPs

Ni and Co NPs in Paper III were prepared via the modified hot injection and heat up methods, respectively. For the synthesis of Ni NPs, a three-

neck round bottom flask containing OAm, TOP and Ni(acac)$_2$ was heated up to 100 °C. After purging the flask with N$_2$ for 30 min, the flask was transferred to another oil bath, which was preheated to 230 °C. The reaction was held for 20 min and then the flask was taken out and cooled down naturally. The resulting Ni NPs were separated by centrifugation at least three times to remove residual surfactants and impurities. The final powder was then collected by drying the sample in nitrogen at room temperature overnight.

For the synthesis of Co NPs, a three-neck round bottom flask containing DCB, TOPO and OA was heated up to reflux. After purging the flask with N$_2$ for 30 min, Co$_2$(CO)$_8$ dissolved in DCB was rapidly injected into the flask. The reaction was held for 20 min and then the flask was taken out and cooled down naturally. The resulting Co NPs were separated by centrifugation at least three times to remove residual surfactants and impurities. The final powder was then collected by drying the sample in nitrogen at room temperature overnight.

## 4.2.2 Synthesis of supported Ni catalysts

In Paper V, the supported Ni catalysts were prepared via the modified polyol method. For the preparation of Ni/KB catalyst, a three-neck round bottom flask was added with EG, Ni(NO$_3$)$_2$·6H$_2$O, and KB. The nominal loading of Ni metal was set to 20 wt. %. After dispersing the mixture by ultrasound for 15 min, the flask was sealed, stirred, and purged with N$_2$ for another 30 min. Afterwards, the flask was placed inside an oil bath and heated to 200 °C. When the temperature stabilized at 200 °C, NaBH$_4$ was rapidly added to the flask. The reaction system was kept for another 2 h, and then the flask was taken out and cooled down naturally. The resultant products were separated by centrifugation, washed with ethanol and distilled water (18 MΩ), and dried in N$_2$ flow at room temperature. The other supported Ni catalysts were synthesized in the same way but replacing the KB with the same amount of CNT, GNP, and zeolite, respectively.

### 4.2.3 Synthesis of thiospinel NPs

All sulfide NPs in Paper VI, including NiS, $Co_3S_4$, $NiCo_2S_4$, $CoNi_2S_4$, $NiFe_2S_4$, and $CuCo_2S_4$, were synthesized via the modified heat up method. In a typical synthetic receipt with $NiCo_2S_4$ as an example, a three-neck round bottom flask containing OAm, $Ni(acac)_2$, $Co(acac)_3$ and sulfur (Ni:Co:S in the stoichiometric ratio of 1:2:4) was preheated to 80 °C. After purging the flask with $N_2$ for 30 min, the flask was transferred to another oil bath or heating mantle, which was thermostated at different temperatures. The reaction was held for 1 h and the flask was then taken out and cooled down naturally. The resulting sulfide NPs were separated by centrifugation at least three times to remove residual surfactants and impurities. The final powder was collected by drying the sample in an electronic oven at 60 °C overnight.

### 4.2.4 Synthesis of MoNiS and MoCoS monolayers

All sulfide catalysts in Paper VII were prepared via the modified heat up method. For the synthesis of MoNiS, a three-neck round bottom flask containing OAm, $Mo(CO)_6$, $Ni(acac)_2$ and sulfur was heated up to 80 °C using a heating mantle (Glas-Col, LLC). After purging the flask with $N_2$ for 30 min, temperature of the heating mantle was elevated to 300 °C. The reaction was held for 1 h and the flask was cooled down naturally. Centrifugation was conducted to separate the products at least 3 times to remove residual surfactants and impurities. The final powder was collected by drying the sample in an electronic oven at 60 °C overnight. MoCoS were prepared by replacing $Co(acac)_3$ with the same amount of $Ni(acac)_2$, whereas $MoS_2$ was prepared by using $Mo(CO)_6$ as the only precursor.

## 4.3 Catalyst characterization

Powder X-ray powder diffraction (XRD) was performed to get the crystallographic information of the catalysts. The diffraction patterns

were recorded on a Bruker-AXS Microdiffractometer (D8 ADVANCE) using Cu K$\alpha$ radiation source ($\lambda$ = 1.5406 Å, 40 kV and 40 mA). Scanning angles were set in the 2θ range of 10–90° with a step interval of 2.0 °/min. Peaks were indexed using the database established by Joint Committee on Powder Diffraction Standards (JCPDS).

The microstructures and morphology of catalysts were characterized by transmission electron microscopy (TEM, JEOL JEM-2100F, 200 kV) and scanning electron microscopy (SEM, FEI Helios NanoLab 460HP, 10 kV). Elemental mapping of the catalysts was carried out using an energy dispersive X-ray (EDX) analyzer attached to SEM. For the specimen preparation, one droplet of the suspension was dropped onto a copper grid coated with carbon film (400 mesh, TAAB) and dried in air.

The Raman spectra were obtained by using a JOBIN YVON HR800 laser confocal micro-Raman spectrometer equipped with an optical microscope, a charge-coupled device (CCD) camera, and an argon-ion laser source. The laser provided 50 mW power at $\lambda$ = 514.5 nm for the exciting line.

Fourier-transform infrared spectroscopy (FTIR) was carried out on a Nicolet NEXUS 670 spectrometer by using a deuterated triglycine sulfate detector. All spectra were recorded with a resolution of 4 cm$^{-1}$ for 32 scans in the spectral range between $\tilde{v}$ = 400 and 4000 cm$^{-1}$. The background spectrum of air was measured as a single beam and used as reference.

Thermal gravimetric analysis (TGA) was conducted on the Perkin-Elmer Pyris 1 TGA apparatus at a heating rate of 10 °C min$^{-1}$ from room temperature to 950 °C under 50 mL min$^{-1}$ flowing air atmosphere.

X-ray photoelectron spectroscopy (XPS) analysis was performed on the ESCALAB 250Xi (Thermo Scientific) XPS system utilizing a monochromatic Al K$\alpha$ source (1486.6 eV). High-resolution spectra were obtained at a pass energy of 30.0 eV, a step size of 0.1 eV, and a dwell

time of 500 ms per step. All spectra were referenced to the C 1s peak (284.8 eV).

Nitrogen adsorption–desorption measurements were conducted at the liquid nitrogen temperature of 77 K on a Micromeritics TriStar II surface area and porosity analyzer after degassing under vacuum using a sample degas system (Micromeritics VacPrep 061). Specific surface area (SSA) was calculated using the Brunauer–Emmett–Teller (BET) method. Total pore volume ($PV_{total}$) was measured by using the quantity of gas adsorbed at $P/P_0$ of 0.99. Total mesopore volume ($PV_{meso}$) was determined by the desorption branch of the isotherms using the Barrett–Joyner–Halenda (BJH) method, while total micropore volume ($PV_{micro}$) was obtained using the Horvath–Kawazoe method.

## 4.4 Catalyst evaluation

### 4.4.1 Experimental setup

The HDS reaction in Paper III and IV was performed in a 50 mL Teflon-lined stainless-steel autoclave reactor. Thiophene as the sulfur-containing model compound and tetralin as the hydrogen donor in a total volume of 20 mL together with the catalysts were added into the reactor. No diluting solvent was added and sulfur content in this mixture was relatively high. The Teflon container was then sonicated for 10 min to disperse the catalysts. The mixture was sealed tightly and the reactor was placed inside an electronic oven preheated to 120–180 °C for a duration of 12–48 h. After the reaction, the reactor was cooled down naturally. Reaction products were analyzed to evaluate the HDS activity of catalysts.

The upgrading reactions in Paper V were carried out in a 4564 Parr Mini Bench Top Reactor with a volume capacity of 160 mL. Typically, 30 g of heavy crude oil and 0.1 g of catalyst were loaded to the reactor. After being sealed tightly, the reactor was purged with $H_2$ or $N_2$ for 30 min and

then pressurized to 11 bar with the corresponding gas. Next, the reactor was heated up from room temperature to the designated temperatures. A final pressure in the range of 20–40 bar was reached. The reaction system was held for different reaction periods and cooled down naturally after the reaction. During the whole reaction period, the stirring torque was maintained at half of the full power. Finally, the oil samples were taken out and stored in glass bottles for further analysis.

The HDS and HDN reactions in Paper VI and VII were performed in a 4564 Parr Mini Bench Top Reactor with a volume capacity of 160 mL. Typically, a 40 mL liquid mixture composed of thiophene or pyridine as the model compound, tetralin as the hydrogen donor and hexane solvent in a specific volume ratio, together with 100 mg of catalysts were loaded into the reactor. After being tightly sealed, the reactor was sonicated in an ultrasound bath for 10 minutes to disperse the catalysts. $H_2$ (purity 5.0, Praxair Norge AS) or $N_2$ (purity 2.6, Praxair Norge AS) was used to purge the reactor for 30 minutes and then pressurize it to 11 bar. Afterwards, the reactor was heated up to the designated reaction temperatures and held for 5 h for different reaction periods. A final reactor pressure in the range of 55–60 bar was reached. During the whole reaction period, the stirring torque was maintained at half of the full power. After cooling down naturally, the reactor was depressurized to atmosphere pressure.

## 4.4.2 Analysis of reaction products

Measurement of the thiophene and pyridine content before and after the reaction (Paper III, IV, VI and VII) was carried out on an Agilent 7820 Gas Chromatograph (GC) equipped with a J&W HP-5 column (length 30 m, diameter 0.25 mm, thickness 1.0 μm) and a flame ionization detector (FID). In each analysis, 600 μL of sample liquid from the reactor was diluted with 600 μL of toluene, and this mixture was utilized to measure the thiophene or pyridine concentration. Each sample test was repeated three times on the GC and the average value was taken as the

thiophene or pyridine content. The conversion was calculated according to the following equation

$$\Delta C = \frac{C_0 - C_1}{C_0} \times 100\%$$

where $\Delta C$ was the thiophene or pyridine conversion ratio; $C_0$ and $C_1$ were the thiophene or pyridine concentration before and after the reaction, respectively.

The following analysis was referred to Paper V. Rheological properties of the heavy oil samples were measured on the Anton Paar MCR 302 Rheometer at 30 °C and atmospheric pressure. In the viscosity-shear rate curves, 25 measuring points were taken with the shear rate in the range of 1-100 s$^{-1}$. Viscosity data at the shear rate of 30 s$^{-1}$ was taken to calculate the ratio of viscosity reduction, based on the equation below

$$\Delta\eta = {(\eta_0 - \eta_1)}/{\eta_0} \times 100\%$$

where $\Delta\eta$ was the ratio of viscosity reduction; $\eta_0$ and $\eta_1$ were the viscosities of the original and upgraded oil, respectively.

True boiling point (TBP) distribution was determined on an AC Analytical Controls high-temperature simulated distillation (HT-SimDis) instrument modified with an Agilent 6890N gas chromatograph (GC) in accordance with the ASTM D7169 standard test method. An AC capillary GC column (5 m × 0.53 mm × 0.17 μm) was equipped on the GC. Cumulative mass as a function of the boiling point up to 750 °C of the feedstock was measured. Carbon disulfide was used as the solvent to dissolve the oil sample with concentration in the range of 1-2 wt. %.

The original and upgraded crude oil samples were analyzed by negative-ion electrospray ionization (ESI) Fourier transform ion cyclotron resonance mass spectrometry (FT-ICR MS, Bruker). The MS analysis was carried out on a Bruker Apex-ultra FT-ICR mass spectrometer with

a 9.4 T superconducting magnet. Sample solutions were infused via an Apollo II electrospray source at 180 µL/h with a syringe pump. Data analysis was performed using custom software and the procedure has been described in detail elsewhere. The compounds were characterized by class (numbers of N, O, and S heteroatoms), type (rings plus double bond equivalence, or DBE), and carbon number. Each class species and their isotopes with different DBE and carbon number values were searched within a set ±0.001 Kendrick mass defect tolerance.

Contents of C, H, O, N and S in the oil samples were measured on different instruments. C and H contents were determined on the Elementar (Germany) VARIO EL cube instrument. O content was measured on the Elementar (Germany) rapid OXY cube oxygen analyzer. N and S contents were analyzed on the Analytik Jena (Germany) Multi EA 3100 Micro-Elemental Analyzer.

# 5 Results and Discussion

## 5.1 Monodispersed Ni and Co NPs for HDS (Paper III)

### 5.1.1 Catalyst characterization

To determine the morphology and particle size distribution (PSD) of the NP products, TEM images are recorded together with the corresponding PSD, as shown in Figure 5.1. These spherical NPs are monodispersed and no apparent agglomeration is observed. An average particle size of 6 nm for the Co NPs (Figure 5.1a and b) is calculated and a narrow size distribution is confirmed. Similarly, monodispersed spherical Ni NPs are also observed in Figure 5.1c and e with an average particle size of 9 and 27 nm, respectively. Commercial Co and Ni particles in micron and submicron scale are also used for comparison. The Co samples with different sizes are designated as Co-6, Co-30, and Co-2000 in order of increasing size, whereas Ni samples are similarly designated as Ni-9, Ni-27, Ni-100 and Ni-1000.

The crystal phase and crystallinity of the as-prepared NPs are analyzed by XRD. Figure 5.2 and 5.3 show the diffraction patterns of the Co and Ni samples, respectively. According to the three characteristic peaks at 44.2°, 51.5° and 75.9° in Figure 5.2, both Co-6 and Co-30 NPs can be indexed to cubic $\alpha$-Co phase (JCPDS card No. 89-7093). The high intensity indicates a relatively good crystallinity of the Co-30 NP sample, while the poor peak intensity of the Co-6 NPs indicates either its small particle size as observed from TEM images or its semi-amorphous nature. In addition, the Co-2000 sample presents a hexagonal phase (JCPDS card No. 89-7094). With respect to the Ni samples in Figure 5.3, three characteristic peaks at 44.5°, 51.8° and 76.4° are observed and they are all indexed to cubic Ni phase (JCPDS card No. 04-0850). The exceptionally sharp peaks of the Ni-100 and Ni-1000 samples suggest

that both samples are well crystalline and the particle sizes are large. Comparatively, the peaks of the Ni-9 and Ni-27 NPs are broader and weaker, implying relatively small particle sizes, which are in accordance with the results from TEM characterization.
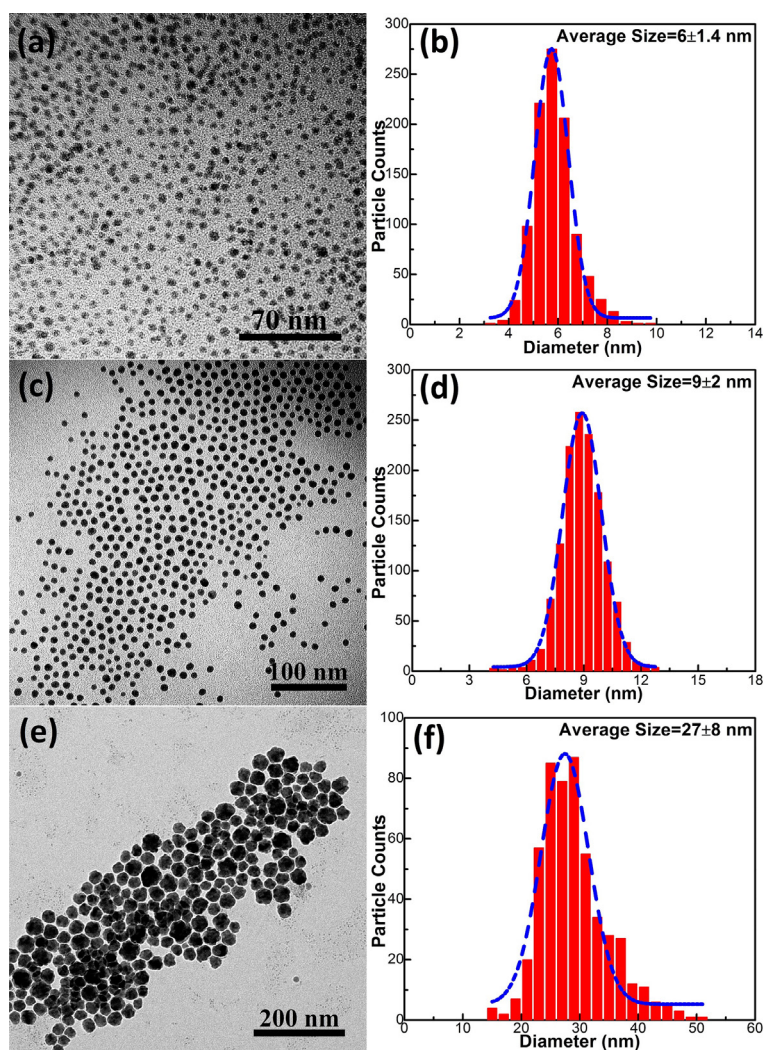


**Figure 5.1** TEM images and corresponding particle size distribution of the as-prepared Co NPs (a, b) and Ni NPs (c, d and e, f).
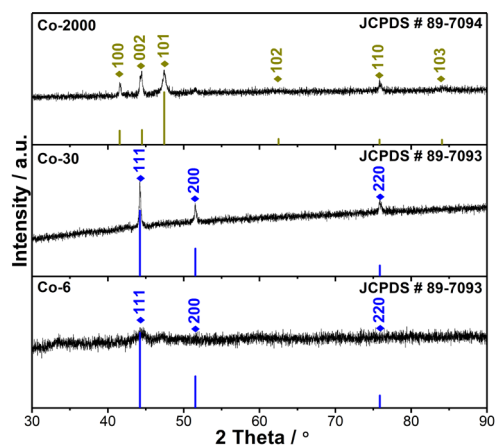
**Figure 5.2** XRD patterns of the Co NPs and commercial Co sample.
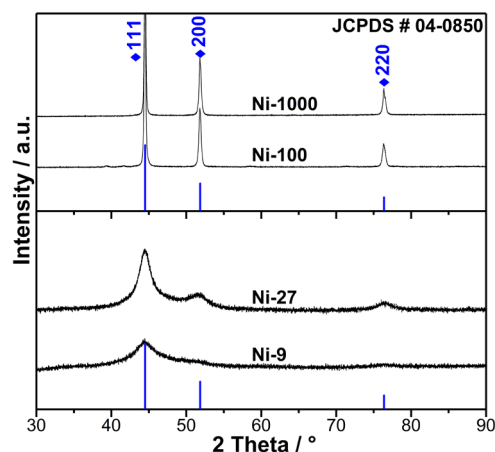


**Figure 5.3** XRD patterns of the Ni NPs and commercial Ni samples.

## 5.1.2 Effect of Ni and Co particle size

Figure 5.4a shows the conversion of three Co catalysts with the same reaction duration of 24 h. Co-6 NPs achieve the highest conversion at all temperatures, compared with the other two Co catalysts. Meanwhile, the conversion increases substantially as the temperature is raised from 160 to 180 °C, indicating that the HDS activity of Co metal is significantly enhanced at elevated temperatures. In Figure 5.4b, the same trend is

observed that the HDS activity is improved with reduced Ni particle size as well as elevated temperature. Specifically, Ni-9 NPs present high thiophene conversion rates of 10.5% and 11.3% at 160 and 180 °C, respectively, which are almost twice as high as that of Co-6 NPs. This suggests that Ni metal displays higher HDS activity than Co at relatively low temperature. Notably, the conversion is almost stable when further increasing the temperature from 160 to 180 °C, suggesting that for Ni catalysts, further increase of temperature does not result in large activity enhancement. Since Co and Ni catalysts exhibit different temperature-activity trends, it could be speculated that the catalytic reactions for the two metallic NPs might follow different reaction pathways and Ni NPs exhibit higher HDS activity than Co NPs.
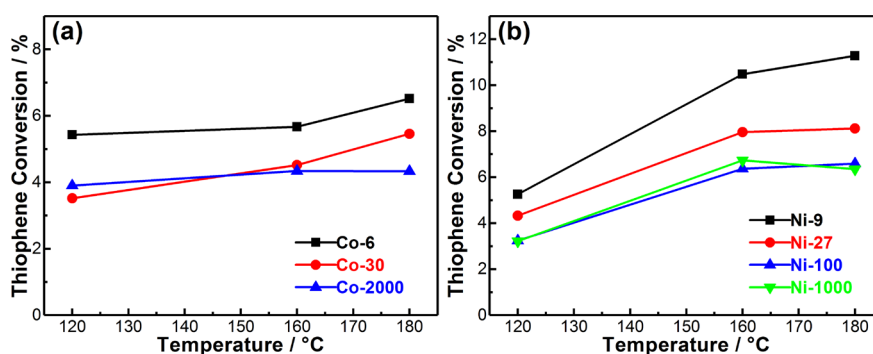


**Figure 5.4** Thiophene conversion of all Co (a) and Ni (b) samples at different temperatures of 120, 160 and 180 °C.

## 5.1.3 Effect of reaction time

HDS reaction with Ni catalysts of four different sizes are performed for reaction periods of 12, 24 and 48 h to study effect of reaction time. As shown in Figure 5.5, substantial increase of the conversion is observed for all Ni catalysts when extending the time from 12 to 24 h. Afterwards, the conversions remain unchanged except that conversion over Ni-9 NPs is slightly improved to 11.9% when prolonging the reaction time to 48 h. This result reveals that the reaction time can be optimized to reach the desirable HDS activity of NP catalysts.
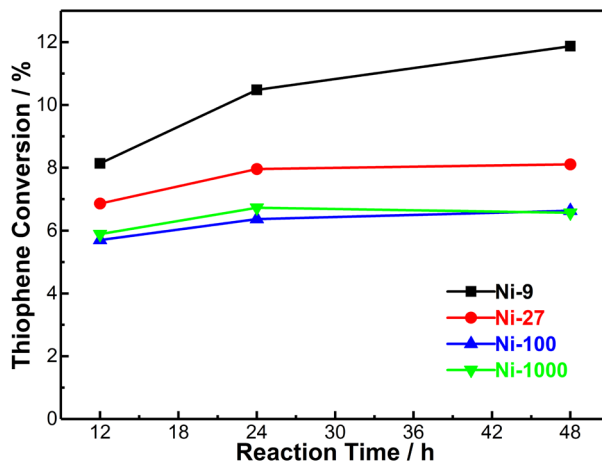
**Figure 5.5** Thiophene conversion of four Ni catalysts with different reaction durations of 12, 24 and 48 h at temperature of 160 °C.

## 5.1.4 Characterization of spent catalysts

To explain the enhanced HDS activity of Ni NPs, we further conduct TEM analysis of the Co-6, Ni-9 and Ni-27 catalysts after HDS reaction at 160 °C for 24 h. Figure 5.6 shows the TEM images of these three catalysts and the corresponding PSD (insets in Figure 5.6b and c). After the HDS reaction, Co-6 NPs agglomerate into much larger particle sizes, which can explain the activity degradation of Co NPs. On the contrary, well-dispersed NPs can be observed in Figure 5.6b and c for the Ni-9 and Ni-27 catalysts, respectively, although slight aggregation still occurs. PSD curves confirm the average particle sizes of 12 and 31 nm for Ni-9 and Ni-27 NPs, respectively, indicating that Ni catalysts are relatively stable in the HDS reaction. These results suggest that the as-prepared Ni NPs display better stability than the Co NPs. The high stability of the Ni NPs at reaction temperature ensures their high HDS activity at reservoir relevant conditions.
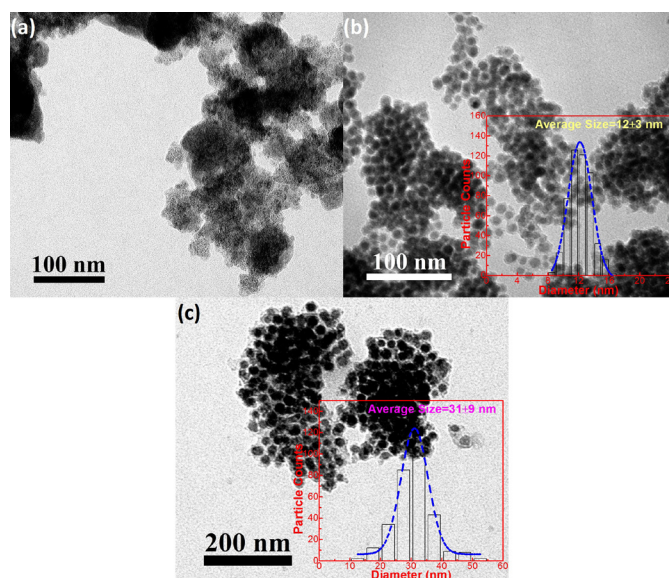
**Figure 5.6** TEM images and corresponding PSD curves (insets) of the Co-6 NPs (a), Ni-9 NPs (b) and Ni-27 NPs (c) after the HDS reaction.

## 5.2 Carbon nanomaterials for HDS (Paper IV)

### 5.2.1 Characterization of carbon materials

Raman spectroscopy is utilized to analyze the carbon allotropes. Figure 5.7 shows the Raman spectra of the carbon samples and Table 5.1 lists the position of D and G bands as well as their intensity ratio ($I_D/I_G$). The band intensity ratio indicates the graphitization degree of carbon materials. KB shows the highest $I_D/I_G$ ratio of 1.87, suggesting the highest disorder. This agrees with the fact that KB is normally stacked of small and disordered graphitic-like sheets. In addition, the $I_D/I_G$ ratio of CNT1 (0.84) is larger than that of CNT2 (0.44), implying CNT2 possesses a higher graphitization than CNT1. With an $I_D/I_G$ ratio of 0.28, GNP gives the best graphitization among the four carbon samples, which is attributed to the nanoplatelet structure composed of multiple and ordered graphitic-like sheets. The 2D band with an asymmetric shape and a low intensity further confirms the nature of multiple layers.
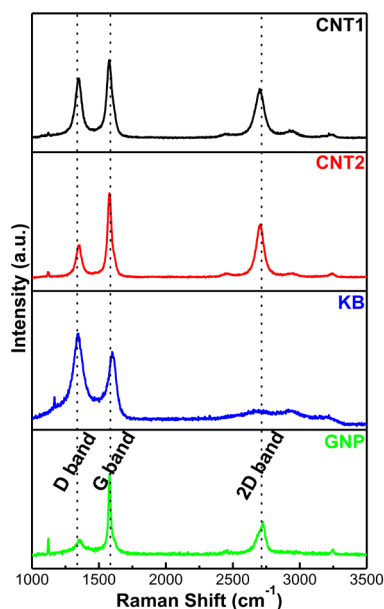
**Figure 5.7** Raman spectra of the carbon nanomaterials.

**Table 5.1** Summary of the Raman spectra results of the carbon materials.

| Carbon nanomaterial | D band position ($cm^{-1}$) | G band position ($cm^{-1}$) | $I_D/I_G$ |
|---|---|---|---|
| CNT1 | 1348 | 1577 | 0.84 |
| CNT2 | 1350 | 1579 | 0.44 |
| KB | 1346 | 1600 | 1.87 |
| GNP | 1351 | 1579 | 0.28 |

TEM is further performed to characterize the morphology of all carbon materials. CNT1 (Figure 5.8a, b) presents smaller outer diameters than CNT2 (Figure 5.8c, d). The CNTs are of good quality as the diameters of the CNTs are uniform. The length of both CNT samples is in micron scale and the multi-walled tubular structure can be confirmed. KB carbon (Figure 5.8e, f) displays the appearance of aggregated nanopellets with the size of tens of nanometers. In addition, these pellets are amorphous, which is in line with the Raman results. In Figure 5.8g and h, stacked

platelet shape of GNP in micron-size is observed. The poor image contrast of these platelets indicates a small thickness.
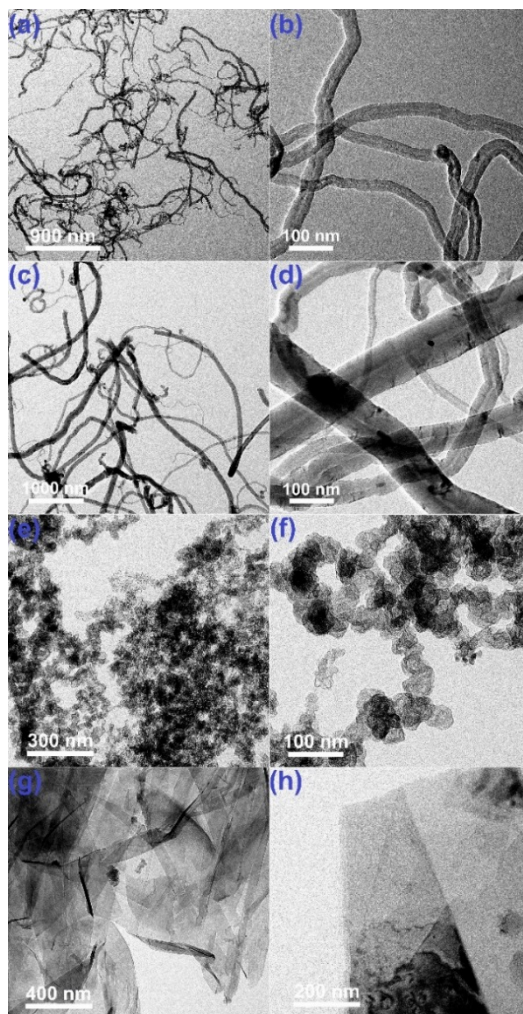


**Figure 5.8** High and low magnification TEM images of CNT1 (a, b), CNT2 (c, d), KB carbon (e, f), and GNP (g, h).

According to the $N_2$ adsorption–desorption isotherms, the BET SSA and BJH PV of the carbon samples are measured, as listed in Table 5.2. KB possesses an ultrahigh SSA of 1339.25 $m^2$/g and a large PV of 1.71 $cm^3$/g, much higher than that of CNTs and GNP.

**Table 5.2** Measured SSA and BJH PV of the carbon materials.

| Carbon nanomaterial | CNT1 | CNT2 | KB | GNP |
|---|---|---|---|---|
| SSA ($m^2/g$) | 113.75 | 57.71 | 1339.25 | 62.51 |
| BJH pore volume ($cm^3/g$) | 0.21 | 0.09 | 1.71 | 0.14 |

FT-IR spectroscopy was performed to characterize the surface functional groups, as shown in Figure 5.9. All samples present four major peaks at similar locations, implying that they have similar surface functional groups. This characteristic allows the fair comparison of their catalytic activity in the HDS reaction. The peaks at 3424, 1635, 1557 and 1103 $cm^{-1}$ reveal that the carboxylic, hydroxyl and unsaturated bond groups are present on the surface of these carbon nanomaterials.
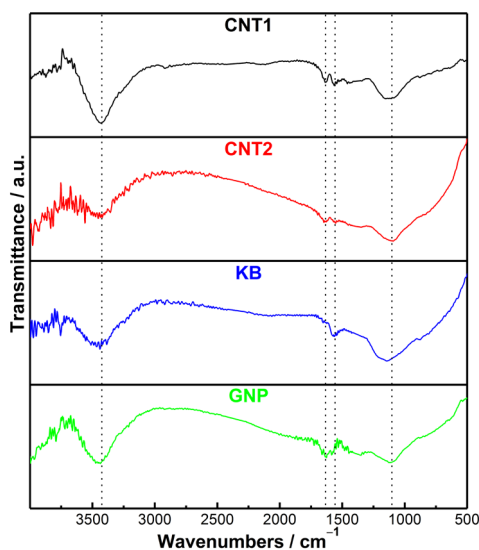


**Figure 5.9** FT-IR spectra of the carbon nanomaterials.

## 5.2.2 Activity of different carbon materials

Figure 5.10 presents the thiophene conversion of the carbon catalysts at temperatures of 120, 160 and 180 °C. Along with elevated temperature,

the conversion rate increases slightly for all catalysts, suggesting that a relatively low temperature of 120 °C is thermodynamically possible to overcome the activation energy of thiophene HDS. At each temperature, the HDS activity is generally in the order of KB > GNP > CNT1 > CNT2. With an ultrahigh SSA, KB carbon is expected to deliver superior activity. However, GNP with a SSA approximately half of CNT1 and same as CNT2 shows surprisingly high activity as well. The catalytic activity of carbon materials is normally correlated with SSA, pore size and PV, and surface functional groups and defects. In addition, electrical and thermal conductivity, which are linked to the graphitization degree, should also be considered. As concluded from the FT-IR spectra, the carbon catalysts present similar surface functional groups with similar intensity. It is thus inferred that both the SSA and the graphitization degree are critical factors dictating the catalytic activity of carbon nanocatalyts in thiophene HDS. As GNP has relatively low SSA and PV while high activity, we further speculate that the high graphitization degree is of paramount importance in the carbon-based HDS reaction.
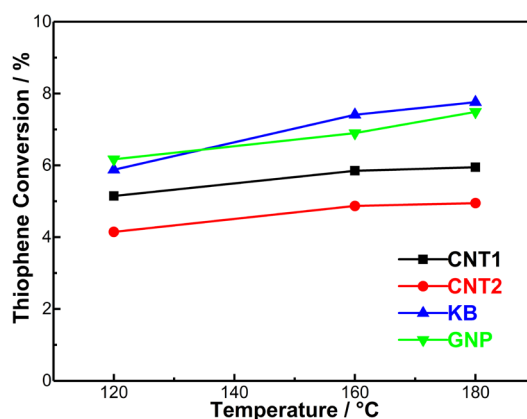


**Figure 5.10** Thiophene conversion with four carbon nanocatalysts at different temperatures of 120, 160 and 180 °C for 24 h.

## 5.3 Carbon supported Ni NPs for heavy oil upgrading (Paper V)

### 5.3.1 Catalyst characterization

The crystal phase structure of the supported catalysts and corresponding supports is characterized by XRD, as shown in Figure 5.11. In all the samples, peaks at 2θ of 44.5°, 51.8° and 76.4° of the supported samples match well with the cubic Ni phase (JCPDS No. 04-0850), confirming the formation of metallic Ni phase. Additionally, the broad peaks of Ni phase in all supported samples imply a relatively small crystal size and the similar peak intensities suggest that the Ni NPs in four samples have close crystal sizes. Based on the Scherrer equation, the mean crystal size of four supported samples is calculated to be around 12 nm.
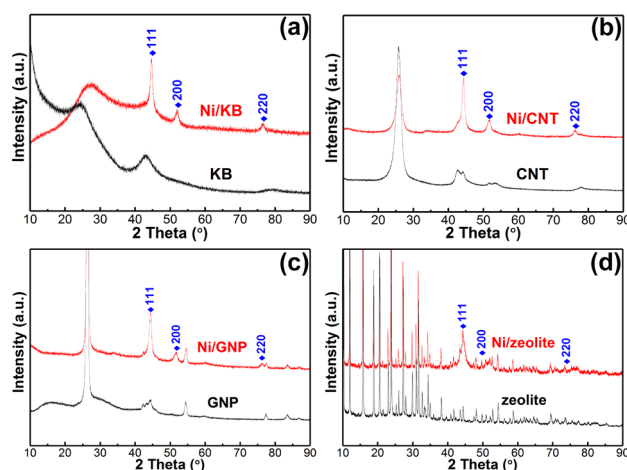


**Figure 5.11** XRD patterns of the (a) KB and Ni/KB, (b) CNT and Ni/CNT, (c) GNP and Ni/GNP, and (d) zeolite and Ni/zeolite samples.

Based on the $N_2$ adsorption–desorption isotherms of four supported samples and the corresponding supports, their SSA, $PV_{total}$, $PV_{meso}$ and $PV_{micro}$ data are obtained, as listed in Table 5.3. Generally, the SSA and PV values of catalysts decrease after loading with Ni NPs. This should be attributed to the pore blocking of carbon by Ni NPs and possible

43

aggregation of the nanospheres in the process of catalyst synthesis. This conclusion is also reflected by the PV data before and after Ni loading. Moreover, for all the carbon and carbon-supported catalysts, $PV_{meso}$ contributes the most to $PV_{total}$, whereas for the zeolite and Ni/zeolite catalysts, $PV_{micro}$ is dominant.

**Table 5.3** SSA and PV data of the supports and supported catalysts.

| | BET SSA $(m^2/g)$ | $PV_{total}$ $(cm^3/g)$ | $PV_{meso}$ $(cm^3/g)$ | $PV_{micro}$ $(cm^3/g)$ |
|---|---|---|---|---|
| KB | 1339.3 | 2.77 | 1.71 | 0.55 |
| CNT | 138.0 | 0.63 | 0.24 | 0.06 |
| GNP | 62.5 | 0.17 | 0.14 | 0.02 |
| zeolite | 635.0 | 0.39 | 0.10 | 0.32 |
| Ni/KB | 827.2 | 1.65 | 1.15 | 0.32 |
| Ni/CNT | 89.9 | 0.36 | 0.16 | 0.04 |
| Ni/GNP | 46.1 | 0.09 | 0.07 | 0.02 |
| Ni/zeolite | 446.4 | 0.34 | 0.11 | 0.23 |

## 5.3.2 Effect of reaction temperature

Figure 5.12a shows the viscosity-shear rate relation measured at 30 °C of the original (heavy crude oil without upgrading) and upgraded oil samples at reaction temperatures of 200, 250, 300 and 350 °C with the Ni/KB catalyst for 2 h in $H_2$. The small viscosity reduction at 200 and 250 °C indicates the catalyst is not active for upgrading at relatively low temperatures. When temperature is elevated to 300 °C, the viscosity is remarkably reduced. With further increase to 350 °C, a significant viscosity reduction is achieved. The viscosity data at a fixed shear rate of 30 $s^{-1}$ is taken to calculate the viscosity reduction ratio. As displayed in Figure 5.12b, the reduction for both 200 and 250 °C are below 30%, much smaller than 75.6% and 97.4% at 300 and 350 °C, respectively.

HT-SimDis measurement is performed to determine the TBP distribution of the upgraded oil samples. Figure 5.12c shows the TBP distribution curves of the original crude oil and upgraded oil samples at four

temperatures. At 200 and 250 °C, the TBP curves almost overlap with that of the original crude oil. When temperature further increases to 300 and 350 °C, the curve is downward shifted gradually, meaning that part of the oil samples are successfully upgraded to products with lower boiling points. Therefore, temperature has a crucial impact on the upgrading of heavy crude oil.
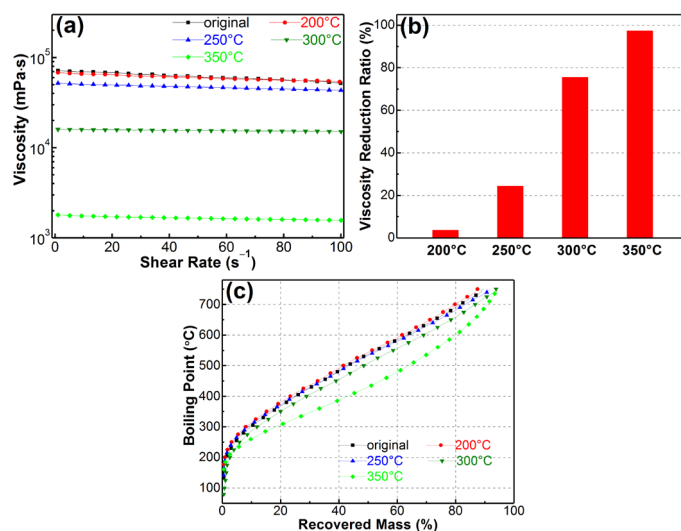


**Figure 5.12** (a) Viscosity at temperature of 30 °C vs shear rate of the original and upgraded heavy crude oils after reaction with Ni/KB catalysts at temperatures of 200, 250, 300 and 350 °C for 2 h in $H_2$, and the corresponding (b) viscosity reduction ratios and (c) TBP distribution curves.

## 5.3.3 Activity of Ni supported catalysts

The four supported catalysts are evaluated in the upgrading reactions at 300 °C for 2 h in $H_2$. Figure 5.13a displays the viscosity reduction with four supported catalysts in comparison with the blank test. The viscosity reduction is in the order of blank < Ni/zeolite < Ni/GNP < Ni/CNT < Ni/KB. The Ni/zeolite with large surface area presents the lowest catalytic activity, which can be ascribed to the inaccessible micropores and possibly aggregated Ni NPs of this catalyst. In addition, the HT-SimDis results in Figure 5.13b show that the TBP distribution curve of oil sample upgraded with Ni/KB is downward shifted by approx. 25 °C

in the temperature range of 400-600 °C, which is attributed to the conversion of heavy and middle end distillates to lighter products.[103] Therefore, it is unanimously shown that the Ni/KB catalyst shows the best activity in decomposing the heavy hydrocarbons.
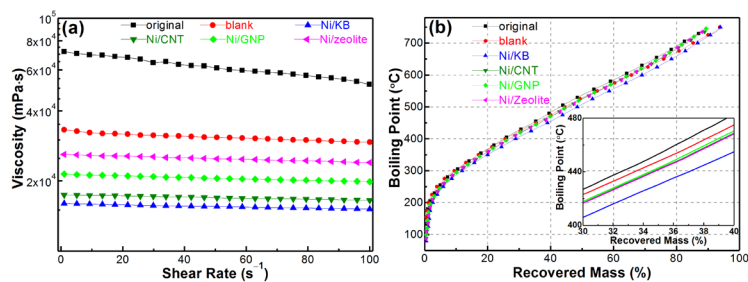


**Figure 5.13** (a) Viscosity at temperature of 30 °C vs shear rate of the original and upgraded heavy crude oils after reaction without catalyst and with Ni/KB, Ni/CNT, Ni/GNP and Ni/zeolite catalysts at 300 °C for 2 h in $H_2$; (b) the corresponding TBP distribution curves.

## 5.3.4 Upgrading reaction mechanism

To understand the upgrading mechanism, we have studied the molecular compositions of heteroatomic compounds in the heavy crude oil samples with the FT-ICR MS technique in the negative-ion mode. Five oil samples, i.e., original, blank test, upgraded with KB at 300 °C, with Ni/KB at 300 and 350 °C, are subjected to this analysis. Based on the spectra, seven major classes of heteroatomic compounds, i.e., $N_1$, $N_1O_1$, $N_1S_1$, $O_1$, $O_1S_1$, $O_2$ and $O_2S_1$, are assigned according to the number and type of heteroatoms. The relative abundance of these seven class species for different oil samples is calculated and presented in Figure 5.14. The column height represents the relative content. Interestingly, when the crude oil is upgraded with Ni/KB at 300 °C, both $O_2$ and $O_2S_1$ class species are markedly reduced. When reaction temperature is further elevated to 350 °C, the relative contents of $O_2$ and $O_2S_1$ class species are significantly reduced. It is therefore concluded that the viscosity reduction of heavy crude oil should be ascribed to the conversion of the $O_2$ and $O_2S_1$ class species, which can be facilitated by the KB catalyst but largely by the Ni/KB catalyst as well as high reaction temperatures.
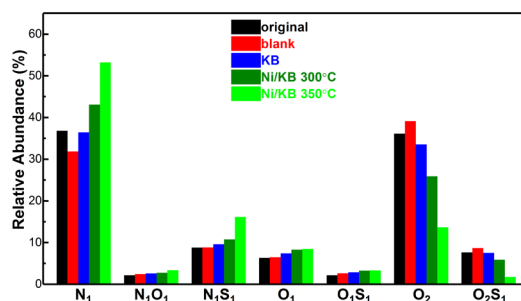
**Figure 5.14** Relative abundance of heteroatom classes assigned from the negative-ion ESI FT-ICR mass spectra of the original and upgraded heavy crude oils after reaction under different conditions.

Elemental analysis is performed to confirm the elemental changes in the upgrading reactions. Table 5.4 shows the contents of C, H, O, N and S of the above-mentioned five oil samples. The C, H, N and S contents in the upgraded oil samples remain nearly the same as the original crude oil, while the O content substantially decreases from 2.10% in the original crude oil to 0.88% in the oil sample upgraded with Ni/KB at 350 °C. The removal of O content is in good agreement with the FT-ICR MS results. S removal has previously been reported to play an important role in the viscosity reduction of heavy crude oil.[23-25,104] Herein, we demonstrate that O removal also contributes importantly to the viscosity reduction of heavy crude oil. Note that the $O_2$ class compounds in heavy crude oil are mainly carboxylic acids, which could be instable and tend to decompose into hydrocarbons and carbon dioxide in the upgrading process.

**Table 5.4** Elemental contents of the original and upgraded heavy crude oils after reaction under different conditions.

| Samples | C (%) | H (%) | O (%) | N (%) | S (%) |
|---|---|---|---|---|---|
| Original crude oil | 83.3 | 10.5 | 2.1 | 0.64 | 3.72 |
| Blank | 83.2 | 10.5 | 1.78 | 0.63 | 3.55 |
| KB | 84 | 10.5 | 1.28 | 0.66 | 3.47 |
| Ni/KB 300 °C | 83.8 | 10.5 | 1.02 | 0.68 | 3.7 |
| Ni/KB 350 °C | 84.7 | 10.1 | 0.88 | 0.69 | 3.45 |

## *5.4   Thiospinel NPs for HDS (Paper VI)*

### *5.4.1 Material characterization*

The TEM image of $NiCo_2S_4$ in Figure 5.15a shows that $NiCo_2S_4$ consists of agglomerated NPs with sizes below 10 nm. TEM images of the NiS, $Co_3S_4$ and $CoNi_2S_4$ samples are displayed in Figures 6.20b-d. NiS consists of well-defined NPs with larger sizes and wider size distribution than that of $NiCo_2S_4$, whereas the poor image contrast of $Co_3S_4$ suggests its semi-amorphous nature. The diffraction rings in the SAED patterns indicate the poor crystallinity of $Co_3S_4$. $CoNi_2S_4$ are also composed of agglomerated NPs and exhibits similar morphology as the $NiCo_2S_4$.
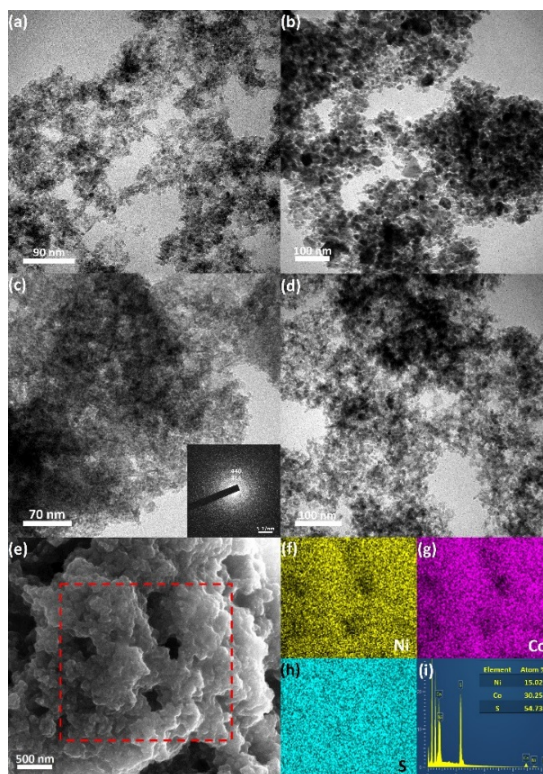


**Figure 5.15** TEM images of the (a) $NiCo_2S_4$, (b) NiS, (c) $Co_3S_4$, and (d) $CoNi_2S_4$ NPs. SEM image (e) of the $NiCo_2S_4$ NPs, and the corresponding elemental mapping of (f) Ni, (g) Co, and (h) S of the red dash area selected from (e), EDX spectra (i) and atomic percentage (inset).

A SEM image of the $NiCo_2S_4$ in Figure 5.15e reveals that these NPs form large aggregates in submicron scale. Elemental mapping of a selected area, as highlighted in Figure 5.15e, and the corresponding EDX spectra (Figure 5.15i) demonstrate that the NPs contain uniformly distributed elements of Ni, Co, and S. The atomic ratio of Ni:Co:S, as listed in inset of Figure 5.15i, is calculated to be approximately 1:2:4, which is consistent with the stoichiometric composition of $NiCo_2S_4$.

The powder XRD patterns for the sulfides are acquired to identify their crystal phases. Figure 5.16a shows the XRD pattern for the $NiCo_2S_4$ NPs. All the characteristic peaks can be indexed to the cubic spinel-type $NiCo_2S_4$ phase (JCPDS No. 20-0782). The broad and weak peaks imply relatively small crystal sizes, in accordance with the result from TEM characterization. It is widely accepted that the $NiCo_2S_4$ thiospinel, which can be derived by substituting the $Co^{2+}$ of $Co_3S_4$ with $Ni^{2+}$, has the normal spinel structure, whereas the $CoNi_2S_4$ thiospinel has the inverse spinel structure.[86,88] In the normal spinel structure of $NiCo_2S_4$, Ni cations occupy the tetrahedral sites while Co cations occupy the octahedral sites.
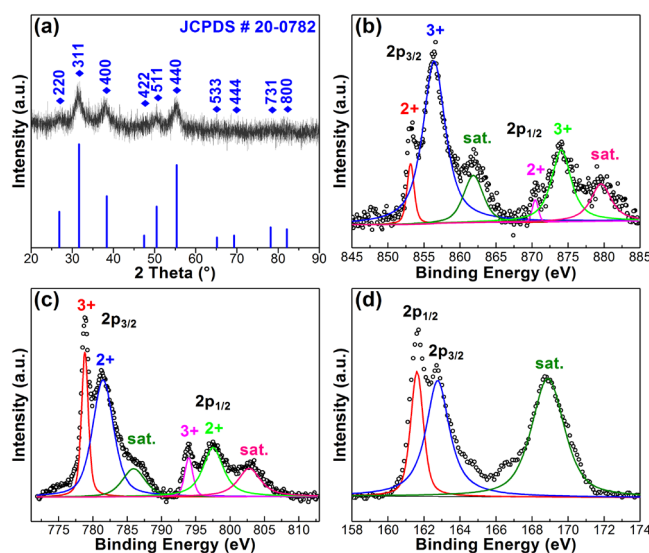


**Figure 5.16** (a) XRD pattern of the $NiCo_2S_4$ NPs. High-resolution XPS spectra of the (b) Ni 2p, (c) Co 2p, and (d) S 2p regions for the $NiCo_2S_4$ NPs.

High-resolution XPS is conducted to investigate the surface species and elemental states of the $NiCo_2S_4$ NPs. By using Gaussian fitting, the Ni 2p spectrum (Figure 5.16b) can be resolved into two spin-orbit doublets and two shakeup satellite peaks (indicated as "sat."). The peaks at 853.1 and 870.4 eV correspond to the $Ni^{2+}$, while the peaks at 856.4 and 874.1 eV belong to the $Ni^{3+}$, indicating the coexistence of $Ni^{2+}$ and $Ni^{3+}$. In the Co 2p spectrum (Figure 5.16c), two spin-orbit doublets and two shakeup satellite peaks are obtained. The peaks at 778.8 and 794.0 eV are indexed to the $Co^{3+}$, while the peaks at 781.5 and 797.5 eV are ascribed to the $Co^{2+}$. The peaks at 161.6 and 162.8 eV in the S 2p spectrum (Figure 5.16d) are attributed to S $2p_{1/2}$ and S $2p_{3/2}$, respectively. These XPS results reveal that the $NiCo_2S_4$ NPs contain $Ni^{2+}$, $Ni^{3+}$, $Co^{2+}$, $Co^{3+}$, and $S^{2-}$, in good agreement with that reported in the literature.[105-106] The surface elemental contents in atomic percentage from the XPS analysis are all consistent with the stoichiometric ratios of the four sulfides.

## 5.4.2 HDS activity of the sulfides

Activity of NiS, $Co_3S_4$, $CoNi_2S_4$, $NiCo_2S_4$, and $MoS_2$ is evaluated in the HDS of thiophene. Figure 5.17 shows the thiophene conversion after the HDS without catalyst and with NiS, $Co_3S_4$, $CoNi_2S_4$, $NiCo_2S_4$, and $MoS_2$. The blank test gives a very low conversion of 1.9 %, indicating thiophene is thermally stable. The higher thiophene conversion exhibited by $Co_3S_4$ relative to the NiS might be attributed to its larger SSA or higher intrinsic activity than that of NiS. Thiophene conversion for $CoNi_2S_4$ NPs is between that of NiS and $Co_3S_4$, implying that Co sulfide might play a more important role in the HDS than Ni sulfide. $NiCo_2S_4$ NPs give a high thiophene conversion of 36.0 %, close to that of $MoS_2$ (39.3 %) as the benchmark HDS catalyst. Note that the SSA of $NiCo_2S_4$ is almost the same as that of $CoNi_2S_4$ and even smaller than that of $Co_3S_4$. It is thus speculated that the activity enhancement exhibited by $NiCo_2S_4$ should originate from its normal spinel structure with Ni and Co cations located on the tetrahedral and octahedral sites, respectively.
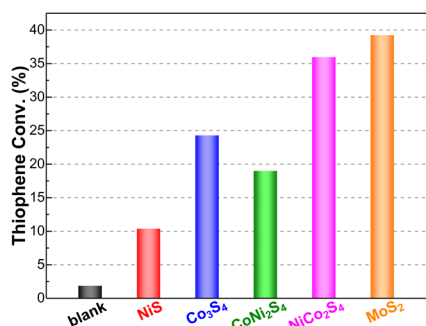
**Figure 5.17** Thiophene conversion of the HDS reaction catalyzed without catalyst and with NiS, $Co_3S_4$, $CoNi_2S_4$, $NiCo_2S_4$, and $MoS_2$.

## 5.4.3 Effect of synthetic temperature

As the synthetic temperature (230 °C) of $NiCo_2S_4$ NPs is lower than the HDS reaction temperature (340 °C), the structural stability of thiospinel NPs is evaluated. Figure 5.18a shows the XRD patterns of the fresh and spent $NiCo_2S_4$ catalysts. After the HDS reaction, a new $Co_9S_8$ phase (JCPDS No. 86-2273) is observed for the spent $NiCo_2S_4$ catalyst. The formation of $Co_9S_8$ phase reveals the deficient structural stability of $NiCo_2S_4$ thiospinels. This instability can be ascribed to the lower synthetic temperature relative to the HDS reaction temperature. The resulting $Co_9S_8$-rich surface is apparently detrimental to the HDS activity of thiospinels.

To elucidate the effect of preparation temperature or essentially the structural stability on the HDS activity, we compare the catalytic performance of $NiCo_2S_4$ NPs prepared at six temperatures of 180, 200, 230, 250, 300, and 350 °C. The XRD patterns in Figure 5.18b reveal that along with the increase of synthetic temperature, the resulting $NiCo_2S_4$ products present slightly higher crystallinity. Figure 5.18c displays the thiophene conversion catalyzed by the six $NiCo_2S_4$ NPs. It can be seen that $NiCo_2S_4$ NPs synthesized at higher temperatures present higher thiophene conversions in the temperature range of 180–350 °C. Particularly, when the synthetic temperature is 350 °C, higher than the

HDS reaction temperature of 340 °C, the highest thiophene conversion of 62.9 % is achieved. Figure 5.18d shows the XRD patterns of fresh and spent $NiCo_2S_4$ prepared at 350 °C. The thiospinel crystal phase remains unchanged, indicating the high structural stability.
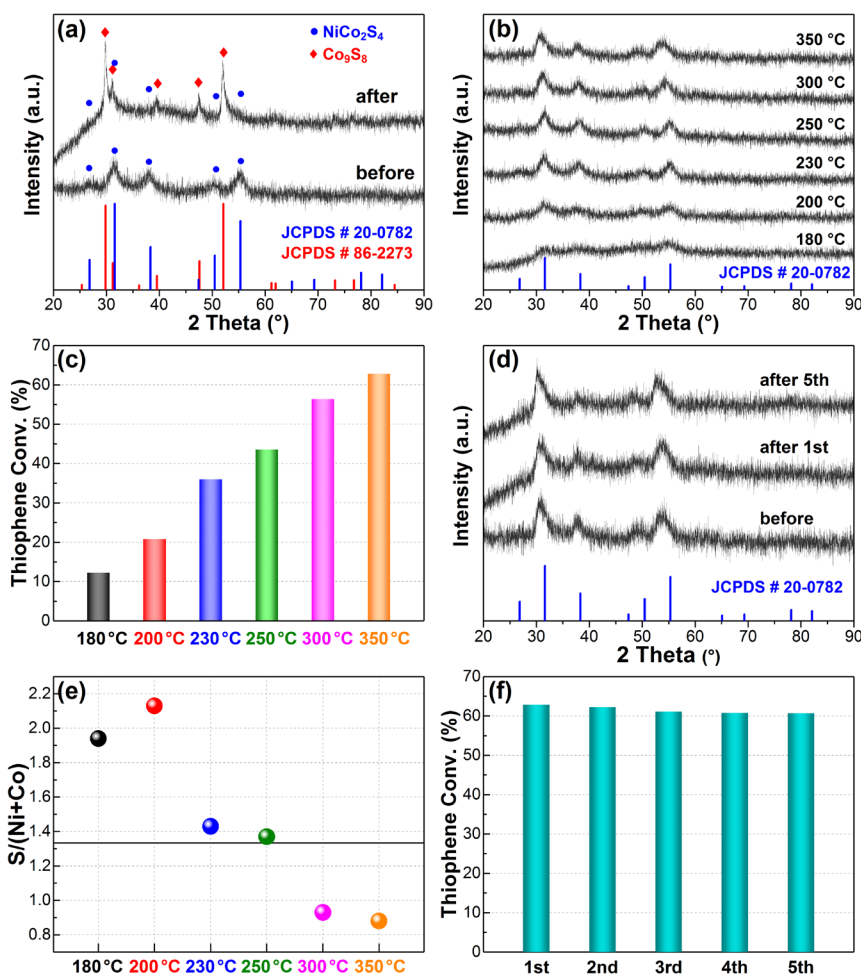


**Figure 5.18** (a) XRD patterns of $NiCo_2S_4$ prepared at 230 °C before and after the HDS reaction. (b) XRD patterns of the $NiCo_2S_4$ prepared at six temperatures. (c) Thiophene conversion of the HDS reaction catalyzed by $NiCo_2S_4$ prepared at six temperatures. (d) XRD patterns of the $NiCo_2S_4$ prepared at 350 °C before, after 1st and after 5th HDS reaction. (e) Content of surface sulfur vacancy expressed by the ratio of sulfur to metal content for $NiCo_2S_4$ prepared at six temperatures. The horizontal line at 1.33 is the stoichiometric value of $NiCo_2S_4$. (f) Thiophene conversion of the HDS reaction catalyzed by $NiCo_2S_4$ prepared at 350 °C for five consecutive cycles.

Furthermore, surface sulfur vacancy is considered as it can contribute as the active sites for sulfur abstraction in thiophene during HDS. According the XPS analysis, the density of surface sulfur vacancy, as expressed by the ratio of S content to metal content, of the six $NiCo_2S_4$ is thus calculated and illustrated in Figure 5.18e. For $NiCo_2S_4$ NPs prepared at relatively low temperatures of 180 and 200 °C, the sulfur content is above the theoretical value of 1.33. Higher synthetic temperature of 230 and 250 °C results in a sulfur content close to 1.33. Whereas, increasing the temperature to 300 and 350 °C leads to a sulfur content below the theoretical value, demonstrating that the sulfur vacancy rich surface of the $NiCo_2S_4$. As such, it is inferred that the synthetic temperature of $NiCo_2S_4$ NPs can greatly affect the structural stability and the density of surface sulfur vacancy of the resulting NPs and thus the HDS activity.

## 5.4.4 Catalyst reusability

The catalyst life of HDS catalysts is another important factor to be considered for potential industrial applications. To this end, we have recycled the $NiCo_2S_4$ NPs synthesized at 350 °C for five consecutive HDS reactions. Figure 5.18f shows the thiophene conversion for five HDS runs. After five cycles, a high thiophene conversion of 60.7 % is retained with only a slight activity loss of 3.5 %, suggesting a remarkable reusability of the $NiCo_2S_4$ catalysts. XRD pattern of the spent $NiCo_2S_4$ catalyst after five runs, as shown in Figure 5.18d, is compared with that of the $NiCo_2S_4$ catalyst before and after first cycle. The similar peak intensities again demonstrate the excellent structural stability of $NiCo_2S_4$ catalyst synthesized at 350 °C. These results prove that the $NiCo_2S_4$ thiospinel NPs with high stability and activity are promising catalysts for industrial HDS processes.

## 5.5 MoNiS and MoCoS monolayers for HDS and HDN (Paper VII)

### 5.5.1 Material characterization

The morphology of the $MoS_2$, MoNiS and MoCoS is analyzed by TEM, as shown in Figure 5.19a, b and c, respectively. The monolayer structure in random orientation can be clearly observed from the side view for all the $MoS_2$-based sulfides. A portion of the monolayers is found distorted, indicating a defect-rich structure of these sulfides. Meanwhile, the absence of in-plane lattice fringes suggests that the three sulfides have low crystallinity. Figure 5.19d, e and f presents the lateral size distributions of the $MoS_2$, MoNiS and MoCoS monolayers, respectively. It can be seen that the $MoS_2$, MoNiS and MoCoS have very close average lateral sizes of 4.31±0.04, 4.15±0.12 and 4.55±0.14 nm. The ultrasmall lateral sizes indicate the high content of active edge sites in the sulfides, which is desirable for their catalytic applications. The commercial $MoS_2$ (c-$MoS_2$) with an average particle size of 90 nm is used as a reference.
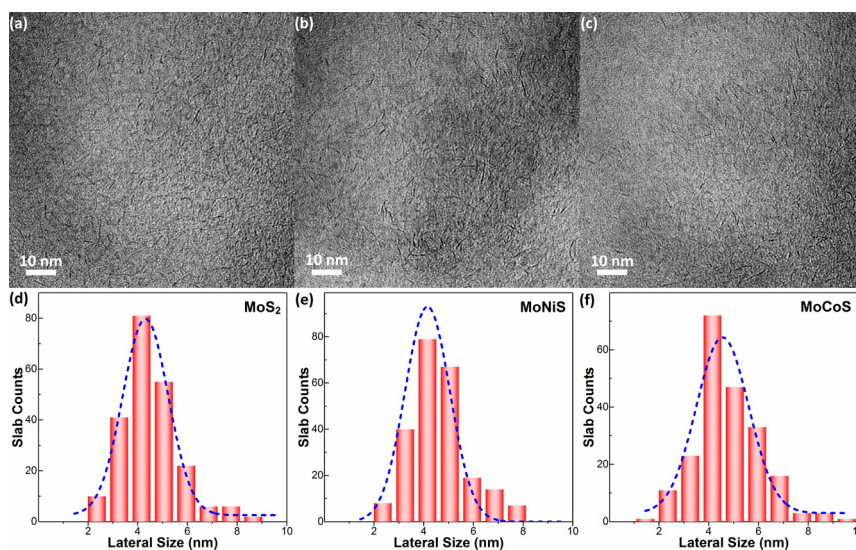


**Figure 5.19** TEM images and corresponding lateral size distribution curves with Gaussian fits of the $MoS_2$ (a, d), MoNiS (b, e) and MoCoS (c, f).

XRD characterization is carried out to examine the composition and crystal phase of the sulfides. Figure 5.20 shows that the sulfides display similar diffraction pattern and the identified diffraction peaks can be indexed to the hexagonal 2H–$MoS_2$ phase (JCPDS card No. 37-1492). The weak intensity of peaks at 32.7 and 58.3°, corresponding to the (100) and (110) in-plane diffraction, indicates the poor crystallinity. The absence of the (002) characteristic peak at 14.3° suggests no evident stacking of the $MoS_2$ monolayers along the *c*-axis. These results accord well with that observed from the TEM characterization.
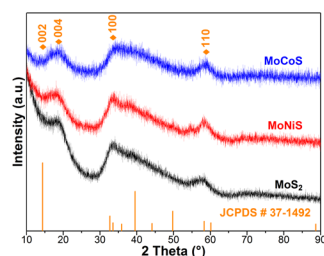


**Figure 5.20** XRD patterns of the $MoS_2$, MoNiS and MoCoS.

## 5.5.2 Individual HDS and HDN

The catalytic activity of c-$MoS_2$, $MoS_2$, MoNiS and MoCoS for the HDS and HDN is evaluated individually using thiophene and pyridine as the model compounds. Figure 5.21a shows the thiophene conversion after the HDS without catalyst and with c-$MoS_2$, $MoS_2$, MoNiS, and MoCoS at different time points. The blank test for 5 h gives a very low conversion of 1.1 %, suggesting the high thermal stability of thiophene, whereas a conversion of 22.7 % is obtained by the c-$MoS_2$. When $MoS_2$ are introduced in the HDS, thiophene conversion is significantly enhanced. After reaction for 5 h, a thiophene conversion of 63.8 % is achieved. The strong activity enhancement compared to the multilayer c-$MoS_2$ should be attributed to the much higher density of active edge sites of the ultrafine $MoS_2$ monolayers. When either MoNiS or MoCoS is employed as the catalyst, even higher thiophene conversions (above 80 % after 5 h) are obtained compared to that of $MoS_2$, validating the promoting effect

of the Ni and Co atoms. Nonetheless, the small conversion increment exhibited by MoCoS relative to that of MoNiS reveals that Co is a slightly better promoter than Ni in the HDS reaction. Assuming that the HDS of thiophene is a pseudo-first-order reaction, the residual thiophene concentration (i.e., 1-conv.) in logarithmic scale is lineally fitted with reaction time, as displayed in Figure 5.21b. The line slope represents the reaction rate constant. It can be seen that the HDS reaction kinetics is the fastest with MoCoS compared to that with MoNiS and $MoS_2$.
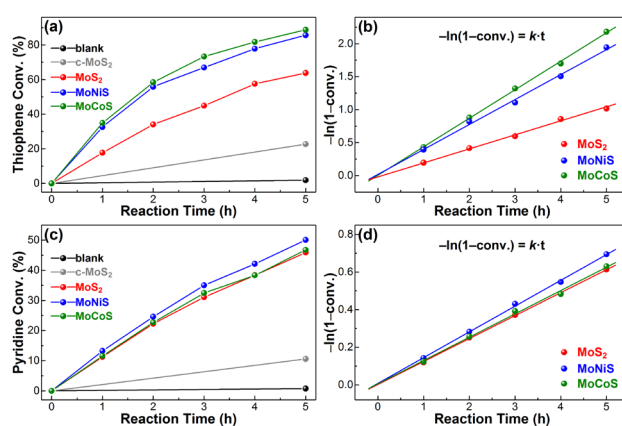


**Figure 5.21** (a) Thiophene conversion of the HDS reaction without catalyst and with $MoS_2$, MoNiS and MoCoS for different times. (b) Corresponding kinetic study of the HDS. (c) Pyridine conversion of the HDN reaction without catalyst and with $MoS_2$, MoNiS and MoCoS for different times. (d) Corresponding kinetic study of the HDN.

The $MoS_2$, MoNiS and MoCoS catalysts are further studied in the HDN of pyridine. Figure 5.21c shows the pyridine conversion over the time course. The blank test indicates that pyridine is also thermally stable. The c-$MoS_2$ gives a relatively low pyridine conversion of 10.6 % after 5 h. However, the conversion increases substantially in the presence of $MoS_2$, MoNiS or MoCoS. The difference of pyridine conversion among them is small and largely the same for $MoS_2$ and MoCoS. MoNiS presents a slightly higher conversion compared with the other two. This finding is also supported by the comparison of the reaction rate constants, as presented in Figure 5.21d. It is thus concluded that Ni is more effective promoter than Co for the HDN reaction.

## 5.5.3 Simultaneous HDS and HDN

To simulate practical hydrotreating processes, we further investigate the catalytic activity of $MoS_2$, MoNiS and MoCoS in the simultaneous HDS and HDN by combining the model compounds. A solution consisting of thiophene, pyridine, tetralin, and hexane in the volume ratio of 0.5:0.2:9:10.3 is used as the feedstock. Figure 5.22 presents the thiophene and pyridine conversion for the simultaneous and individual HDS and HDN catalyzed by $MoS_2$, MoNiS and MoCoS. The front row represents the simultaneous reaction, while the back row are data taken from the individual HDS and HDN in Figure 5.21. It can be observed that for all the three catalysts, the thiophene conversions (red columns) are reduced in the simultaneous reaction in comparison with the individual HDS, whereas pyridine conversions (blue columns) increases obviously from the individual to the simultaneous reaction. The decreased HDS activity can be explained by the more favorable surface adsorption of pyridine molecules over the thiophene molecules to the active sites of the catalysts when both of them are present in the reactant solution, demonstrating the potential role of the nitrogen-containing compounds as a competitive inhibitor. Meanwhile, the increasing pyridine conversion should be attributed to its reduced concentration in the feedstock. Notably, MoNiS exhibits the best catalytic performance with both high thiophene and pyridine conversions of 70.8 and 73.8 % compared to MoCoS and $MoS_2$.
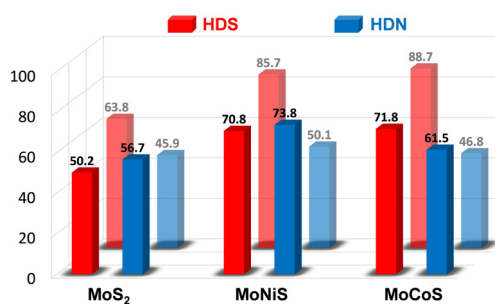


**Figure 5.22** Thiophene and pyridine conversions of the simultaneous (front row) and individual (back row) HDS and HDN reactions catalyzed by $MoS_2$, MoNiS and MoCoS.

57

## 5.5.4 Catalyst reusability

Catalyst reusability is an important factor for industrial applications. To this end, MoCoS and MoNiS, which show highest activity in the HDS and HDN, are tested in individual reaction for five consecutive cycles. Figure 5.23a shows the thiophene conversion of the HDS catalyzed by MoCoS and the pyridine conversion of the HDN catalyzed by MoNiS. No appreciable activity loss is observed for both catalysts after five cycles, indicating the excellent reusability of the MoCoS and MoNiS monolayer catalysts. XRD patterns of the spent MoCoS and MoNiS catalysts after five cycles are compared with that of the fresh ones, as shown in Figure 5.23b and c. It can be seen that the characteristic peak at 32.7 °, corresponding to the (100) basal plane, is intensified after five runs for both the MoNiS and MoCoS catalysts, indicating the increasing in-plane crystallinity during the HDS and HDN reactions. However, no major (002) diffraction peaks are observed for both the spent catalysts, manifesting that no stacking along the *c*-axis occurs and the monolayer structure of MoNiS and MoCoS is well maintained throughout the tests. These results demonstrate the excellent structural stability of the MoNiS and MoCoS monolayers.
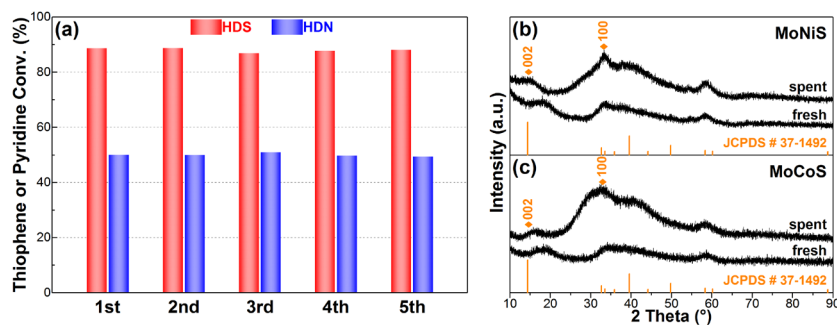


**Figure 5.23** (a) Thiophene and pyridine conversions for the MoCoS and MoNiS for five consecutive cycles. The XRD patterns of the fresh and spent MoNiS (b) and MoCoS (c) after five cycles.

# 6 Concluding Remarks

## *6.1 Conclusions*

In the aquathermolysis of heavy crude oil, HDS is an important reaction involved in the upgrading process. The size-dependent activity has been demonstrated for both Ni and Co NPs. It turns out that Ni metallic NPs exhibit better activity in the activation of C–S bond than the Co NPs, which can be attributed to the inherent activity and high thermal stability in the HDS. Paper III demonstrates the opportunity for the application of well-dispersed metallic NPs in the *in-situ* upgrading and recovery of heavy crude oil under reservoir relevant conditions.

Paper IV showed that KB carbon with an ultrahigh SSA and GNPs with high degree of graphitization exhibited similar HDS activities that were much better than that of CNTs. It has been proposed that the degree of graphitization of carbon nanocatalysts is of great importance in HDS reactions. This study demonstrates the interesting application of carbon nanomaterials as metal-free catalysts in the *in-situ* upgrading and recovery of heavy crude oil.

In Paper V, we found that KB exhibits slightly better activity in the upgrading of heavy oil compared with CNT, GNP, and zeolite supports, while the activity of four supported catalysts varies greatly in the order of Ni/KB > Ni/CNT > Ni/GNP > Ni/zeolite. Synergistic effect between the metal and support is confirmed by the enhanced activity of Ni/KB relative to KB. The viscosity reduction of heavy oil is mainly attributed to the decomposition of carboxylic acids, and the Ni/KB catalyst can effectively catalyze this decomposition reaction. Therefore, the Ni/C catalysts can be potentially applied in the *in-situ* upgrading and recovery of heavy crude oil, especially for oils with high oxygen content.

Paper VI revealed that the high HDS activity exhibited by $NiCo_2S_4$ NPs is linked to the normal thiospinel structure with Ni and Co cations

occupying the tetrahedral and octahedral sites, respectively. We also found that high synthetic temperature endows the $NiCo_2S_4$ thiospinels with high structural stability and abundant surface sulfur vacancy, leading to excellent activity and reusability.

Paper VII reported the synthesis of monolayer $MoS_2$, MoNiS and MoCoS with similar ultrafine lateral sizes as improved HDS and HDN catalysts due to the high density of active sites endowed by the ultrafine monolayer structure. It is also found that Co acts as a slightly better promoter than Ni in the HDS but the opposite in the HDN. Simultaneous HDS and HDN reactions reveals that the nitrogen-containing compounds can serve as a competitive inhibitor for the sulfur-containing compounds because the former binds more strongly to the active sites of catalysts than the latter.

## *6.2   Future work*

Although the Ni and Co NPs present considerable activity in the HDS, their transport behavior in porous medium is to be studied. Further investigation is also needed to clarify the specific roles of critical factors, such as SSA and degree of graphitization, as well as surface functional groups, on the catalytic activity of carbon nanocatalysts. Core flooding experiments with the Ni/C catalysts should be conducted to test the performance in the recovery and upgrading of heavy oil. Based on the importance of structural stability and surface composition for the potential application of thiospinel NPs as HDS catalyst, future study of supported $NiCo_2S_4$ catalysts can be an effective way to enhance their HDS catalytic activity. Key insights in the structure-induced activity enhancement and the scalable synthesis of $MoS_2$-based monolayers for HDS and HDN also warrant further efforts.

# Bibliography

(1) Countries, O. o. t. P. E. *World Oil Outlook 2014*, OPEC: Vienna, Austria, 2014; p 396.

(2) Dusseault, M. B.; Shafiei, A. Oil Sands. In *Ullmann's Encyclopedia of Industrial Chemistry*; Wiley-VCH Verlag GmbH & Co. KGaA: 2000.

(3) Huc, A.-Y. *Heavy Crude Oils: From Geology to Upgrading : An Overview*, Editions Technip: Paris, France, 2011.

(4) Speight, J. G. *Enhanced Recovery Methods for Heavy Oil and Tar Sands*, Gulf Publishing Company: Houston, Texas, 2009; p 370.

(5) Speight, J. G. *Heavy and Extra-Heavy Oil Upgrading Technologies*, Gulf Professional Publishing: USA, 2013.

(6) Muraza, O.; Galadima, A. Aquathermolysis of Heavy Oil: A Review and Perspective on Catalyst Development. *Fuel* **2015,** *157*, 219-231.

(7) Zhao, D. W.; Wang, J. J.; Gates, I. D. An Evaluation of Enhanced Oil Recovery Strategies for a Heavy Oil Reservoir after Cold Production with Sand. *Int. J. Energy Res.* **2015,** *39*, 1355-1365.

(8) Thomas, S. Enhanced Oil Recovery - an Overview. *Oil & Gas Science and Technology - Revue de l'IFP* **2007,** *63*, 9-19.

(9) Zhao, D. W.; Wang, J.; Gates, I. D. Thermal Recovery Strategies for Thin Heavy Oil Reservoirs. *Fuel* **2014,** *117*, 431-441.

(10) Sara Thomas, S. M. F. A. Status and Assessment of Chemical Oil Recovery Methods. *Energy Sources* **1999,** *21*, 177-189.

(11) Homsy, G. Viscous Fingering in Porous Media. *Annu. Rev. Fluid Mech.* **1987,** *19*, 271-311.

(12) Shah, A.; Fishwick, R.; Wood, J.; Leeke, G.; Rigby, S.; Greaves, M. A Review of Novel Techniques for Heavy Oil and Bitumen Extraction and Upgrading. *Energy Environ. Sci.* **2010,** *3*, 700-714.

(13) Alvarado, V.; Manrique, E. Enhanced Oil Recovery: An Update Review. *Energies* **2010,** *3*, 1529-1575.

(14) Zolotukhin, A. B.; Bokserman, A.; Kokorev, V.; Nevedeev, A.; Ushakova, A.; Shchekoldin, K., New Upstream and Downstream Technologies for Extra Heavy Oils. In *SPE Heavy Oil Conference Canada*, Society of Petroleum Engineers: Calgary, Alberta, Canada, 2012.

(15) Dehghan, A. A.; Masihi, M.; Ayatollahi, S. Interfacial Tension and Wettability Change Phenomena During Alkali–Surfactant Interactions with Acidic Heavy Crude Oil. *Energy Fuels* **2015,** *29*, 649-658.

(16) Dong, M.; Ma, S.; Liu, Q. Enhanced Heavy Oil Recovery through Interfacial Instability: A Study of Chemical Flooding for Brintnell Heavy Oil. *Fuel* **2009,** *88*, 1049-1056.

(17) Zhang, H.; Dong, M.; Zhao, S. Which One Is More Important in Chemical Flooding for Enhanced Court Heavy Oil Recovery, Lowering Interfacial Tension or Reducing Water Mobility? *Energy Fuels* **2010,** *24*, 1829-1836.

(18) Mohammed, M.; Babadagli, T. Wettability Alteration: A Comprehensive Review of Materials/Methods and Testing the Selected Ones on Heavy-Oil Containing Oil-Wet Systems. *Adv. Colloid Interface Sci.* **2015,** *220*, 54-77.

(19) Guo, K.; Li, H.; Yu, Z. In-Situ Heavy and Extra-Heavy Oil Recovery: A Review. *Fuel* **2016,** *185*, 886-902.

(20) Guo, K.; Li, H.; Yu, Z. Metallic Nanoparticles for Enhanced Heavy Oil Recovery: Promises and Challenges. *Energy Procedia* **2015,** *75*, 2068-2073.

(21) Hyne, J. B.; Greidanus, J. W.; Tyrer, J. D.; Verona, D.; Rizek, C.; Clark, P. D.; Clarke, R. A.; Koo, J., Aquathermolysis of Heavy Oils. In *the Second International Conference on Heavy Crude and Tar Sands*, Caracas, Venezuela, 1982; Vol. II, pp 25-30.

(22) Rivas, O. R.; Campos, R. E.; Borges, L. G., Experimental Evaluation of Transition Metals Salt Solutions as Additives in Steam Recovery Processes. In *SPE Annual Technical Conference and Exhibition*, Society of Petroleum Engineers: Houston, Texas, 1988.

(23) Clark, P. D.; Hyne, J. B. Chemistry of Organosulphur Compound Types Occurring in Heavy Oil Sands: 3. Reaction of Thiophene and Tetrahydrothiophene with Vanadyl and Nickel Salts. *Fuel* **1984,** *63*, 1649-1654.

(24) Clark, P. D.; Dowling, N. I.; Hyne, J. B.; Lesage, K. L. The Chemistry of Organosulphur Compound Types Occurring in Heavy Oils: 4. The High-Temperature Reaction of Thiophene and Tetrahydrothiophene with Aqueous Solutions of Aluminium and First-Row Transition-Metal Cations. *Fuel* **1987,** *66*, 1353-1357.

(25) Clark, P. D.; Dowling, N. I.; Lesage, K. L.; Hyne, J. B. Chemistry of Organosulphur Compound Types Occurring in Heavy Oil Sands: 5.

Reaction of Thiophene and Tetrahydrothiophene with Aqueous Group Viiib Metal Species at High Temperature. *Fuel* **1987,** *66*, 1699-1702.

(26) Li, J.; Chen, Y.; Liu, H.; Wang, P.; Liu, F. Influences on the Aquathermolysis of Heavy Oil Catalyzed by Two Different Catalytic Ions: $Cu^{2+}$ and $Fe^{3+}$. *Energy Fuels* **2013,** *27*, 2555-2562.

(27) Wen, S.; Zhao, Y.; Liu, Y.; Hu, S., A Study on Catalytic Aquathermolysis of Heavy Crude Oil During Steam Stimulation. In *International Symposium on Oilfield Chemistry*, Society of Petroleum Engineers: Houston, Texas, U.S.A., 2007.

(28) Zhao, X.; Tan, X.; Liu, Y. Behaviors of Oil-Soluble Catalyst for Aquathermolysis of Heavy Oil. *Ind. Catal.* **2008,** *16*, 31-34.

(29) Yi, Y.; Li, S.; Ding, F.; Yu, H. Change of Asphaltene and Resin Properties after Catalytic Aquathermolysis. *Pet. Sci.* **2009,** *6*, 194-200.

(30) Xu, H.; Pu, C.; W, F. Mechanism of Underground Heavy Oil Catalytic Aquathermolysis. *J. Fuel Chem. Technol.* **2012,** *40*, 1206-1211.

(31) Zhao, F.; Liu, Y.; Wu, Y.; Zhao, X.; Tan, L. Study of Catalytic Aquathermolysis of Heavy Oil in the Presence of a Hydrogen Donor. *Chem. Technol. Fuels Oils* **2012,** *48*, 273-282.

(32) Zhao, F.; Wang, X.; Wang, Y.; Y, Shi. The Catalytic Aquathermolysis of Heavy Oil in the Presence of a Hydrogen Donor under Reservoirs Conditions. *J. Chem. Pharm. Res.* **2014,** *6*, 2037-2041.

(33) Petrukhina, N. N.; Kayukova, G. P.; Romanov, G. V.; Tumanyan, B. P.; Foss, L. E.; Kosachev, I. P.; Musin, R. Z.; Ramazanova, A. I.; Vakhin, A. V. Conversion Processes for High-Viscosity Heavy Crude Oil in Catalytic and Noncatalytic Aquathermolysis. *Chem. Tech. Fuels Oils* **2014,** *50*, 315-326.

(34) Zhao, F.; Liu, Y.; Fu, Z.; Zhao, X. Using Hydrogen Donor with Oil-Soluble Catalysts for Upgrading Heavy Oil. *Russ. J. Appl. Chem.* **2015,** *87*, 1498-1506.

(35) Galukhin, A. V.; Erokhin, A. A.; Nurgaliev, D. K. Effect of Catalytic Aquathermolysis on High-Molecular-Weight Components of Heavy Oil in the Ashal'cha Field. *Chem. Technol. Fuels Oils* **2015,** *50*, 555-560.

(36) Chen, Y.; Wang, Y.; Wu, C.; Xia, F. Laboratory Experiments and Field Tests of an Amphiphilic Metallic Chelate for Catalytic Aquathermolysis of Heavy Oil. *Energy Fuels* **2008,** *22*, 1502-1508.

(37) Chen, Y.; Yang, C.; Wang, Y. Gemini Catalyst for Catalytic Aquathermolysis of Heavy Oil. *J. Anal. Appl. Pyrol.* **2010,** *89*, 159-165.

(38) Chao, K.; Chen, Y.; Liu, H.; Zhang, X.; Li, J. Laboratory Experiments and Field Test of a Difunctional Catalyst for Catalytic Aquathermolysis of Heavy Oil. *Energy Fuels* **2012,** *26*, 1152-1159.

(39) Wang, Y.; Chen, Y.; He, J.; Li, P.; Yang, C. Mechanism of Catalytic Aquathermolysis: Influences on Heavy Oil by Two Types of Efficient Catalytic Ions: $Fe^{3+}$ and $Mo^{6+}$. *Energy Fuels* **2010,** *24*, 1502-1510.

(40) Wu, C.; Lei, G.; Yao, C.; Jia, X., In Situ Upgrading Extra-Heavy Oil by Catalytic Aquathermolysis Treatment Using a New Catalyst Based Anamphiphilic Molybdenum Chelate. In *International Oil and Gas Conference and Exhibition in China*, Society of Petroleum Engineers: Beijing, China, 2010.

(41) Wu, C.; Lei, G.; Yao, C.; Sun, K.; Gai, P.; Cao, Y. Mechanism for Reducing the Viscosity of Extra-Heavy Oil by Aquathermolysis with an Amphiphilic Catalyst. *J. Fuel Chem. Technol.* **2010,** *38*, 684-690.

(42) Chao, K.; Chen, Y.; Li, J.; Zhang, X.; Dong, B. Upgrading and Visbreaking of Super-Heavy Oil by Catalytic Aquathermolysis with Aromatic Sulfonic Copper. *Fuel Process Technol.* **2012,** *104*, 174-180.

(43) Wu, C.; Su, J.; Zhang, R.; Lei, G.; Cao, Y. The Use of Amphiphilic Nickel Chelate for Catalytic Aquathermolysis of Extra-Heavy Oil under Steam Injection Conditions. *Energy Sources, Part A* **2014,** *36*, 1437-1444.

(44) Desouky, S.; sabagh, A. A.; Betiha, M.; Badawi, A.; Ghanem, A.; Khalil, S. Catalytic Aquathermolysis of Egyptian Heavy Crude Oil. *Inter. J. Chem. Mater. Sci. Eng.* **2013,** *7*, 286 - 291.

(45) Wang, J.; Liu, L.; Zhang, L.; Li, Z. Aquathermolysis of Heavy Crude Oil with Amphiphilic Nickel and Iron Catalysts. *Energy Fuels* **2014,** *28*, 7440-7447.

(46) Monin, J. C.; Audibert, A. Thermal Cracking of Heavy-Oil/ Mineral Matrix Systems. *SPE Reservoir Eng.* **1988,** *3*, 1243 - 1250.

(47) Fan, H.; Liu, Y.; Zhong, L. Studies on the Synergetic Effects of Mineral and Steam on the Composition Changes of Heavy Oils. *Energy Fuels* **2001,** *15*, 1475-1479.

(48) Fan, H.; Zhang, Y.; Lin, Y. The Catalytic Effects of Minerals on Aquathermolysis of Heavy Oils. *Fuel* **2004,** *83*, 2035-2039.

(49) Ovalles, C.; Vallejos, C.; Vasquez, T.; Rojas, I.; Ehrman, U.; Benitez, J. L.; Martinez, R. Downhole Upgrading of Extra-Heavy Crude

Oil Using Hydrogen Donors and Methane under Steam Injection Conditions. *Petrol. Sci. Technol.* **2003,** *21*, 255-274.

(50) Abu S.M. Junaid; Wei Wang; Christopher Street; Moshfiqur Rahman; Matt Gersbach; Sarah Zhou; William McCaffrey; Kuznicki, S. M. Viscosity Reduction and Upgrading of Athabasca Oilsands Bitumen by Natural Zeolite Cracking. *Inter. J. Chem. Mater. Sci. Eng.* **2010,** *4*, 33-38.

(51) Junaid, A. S. M.; Street, C.; Wang, W.; Rahman, M. M.; An, W.; McCaffrey, W. C.; Kuznicki, S. M. Integrated Extraction and Low Severity Upgrading of Oilsands Bitumen by Activated Natural Zeolite Catalysts. *Fuel* **2012,** *94*, 457-464.

(52) Merissa, S.; Fitriani, P.; Iskandar, F.; Abdullah, M.; Khairurrijal In *Preliminary Study of Natural Zeolite as Catalyst for Decreasing the Viscosity of Heavy Oil*, Padjadjaran International Physics Symposium 2013, Universitas Padjadjaran, West Java-Indonesia, AIP Publishing LLC: Universitas Padjadjaran, West Java-Indonesia, 2013; pp 131-134.

(53) Junaid, A. S. M.; Rahman, M. M.; Rocha, G.; Wang, W.; Kuznicki, T.; McCaffrey, W. C.; Kuznicki, S. M. On the Role of Water in Natural-Zeolite-Catalyzed Cracking of Athabasca Oilsands Bitumen. *Energy Fuels* **2014,** *28*, 3367-3376.

(54) Strausz, O. P.; Mojelsky, T. W.; Payzant, J. D.; Olah, G. A.; Prakash, G. K. S. Upgrading of Alberta's Heavy Oils by Superacid-Catalyzed Hydrocracking. *Energy Fuels* **1999,** *13*, 558-569.

(55) Chen, Y.; Wang, Y.; Lu, J.; Wu, C. The Viscosity Reduction of Nano-Keggin-$K_3PMo_{12}O_{40}$ in Catalytic Aquathermolysis of Heavy Oil. *Fuel* **2009,** *88*, 1426-1434.

(56) Chen, Y.; He, J.; Wang, Y.; Li, P. GC-MS Used in Study on the Mechanism of the Viscosity Reduction of Heavy Oil through Aquathermolysis Catalyzed by Aromatic Sulfonic $H_3PMo_{12}O_{40}$. *Energy* **2010,** *35*, 3454-3460.

(57) Jing, P.; Li, Q.; Han, M.; Sun, D.; Jia, L.; Fang, W. Visbreaking of Heavy Petroleum Oil Catalyzed by $SO_4^{2-}/ZrO_2$ Solid Super-Acid Doped with $Ni^{2+}$ or $Sn^{2+}$. *Front. Chem. Eng. China* **2008,** *2*, 186-190.

(58) Ovalles, C.; Filgueiras, E.; Morales, A.; Rojas, I.; de Jesus, J. C.; Berrios, I. Use of a Dispersed Molybdenum Catalyst and Mechanistic Studies for Upgrading Extra-Heavy Crude Oil Using Methane as Source of Hydrogen. *Energy Fuels* **1998,** *12*, 379-385.

(59) Zhao, F.; Huang, J.; Li, M.; Liu, S.; Guo, Y.; Zhang, P. Study on Hydrogen Donors Catalytic Upgrading of Heavy Oil Using Ultradispersed Catalyst. *J. Chem. Pharm. Res.* **2015,** *7*, 1370-1377.

(60) Ovalles, C.; Filgueiras, E.; Morales, A.; Scott, C. E.; Gonzalez-Gimenez, F.; Pierre Embaid, B. Use of a Dispersed Iron Catalyst for Upgrading Extra-Heavy Crude Oil Using Methane as Source of Hydrogen. *Fuel* **2003,** *82*, 887-892.

(61) Shokrlu, Y. H.; Babadagli, T. Viscosity Reduction of Heavy Oil/Bitumen Using Micro- and Nano-Metal Particles During Aqueous and Non-Aqueous Thermal Applications. *J. Petrol. Sci. Eng.* **2014,** *119*, 210-220.

(62) Yang, Z.; Liu, X.; Su, C.; Li, X.; Zhang, Z.; Zhao, M. Preparation of Silica Supported Nanoscale Zero Valence Iron and Its Feasibility in Viscosity Reduction of Heavy Oil. *Micro Nano Lett.* **2014,** *9*, 355-358.

(63) Li, W.; Zhu, J; Qi, J. Application of Nano-Nickel Catalyst in the Viscosity Reduction of Liaohe Extra-Heavy Oil by Aqua-Thermolysis. *J. Fuel Chem. Technol.* **2007,** *35*, 176-180.

(64) Greff, J.; Babadagli, T. Use of Nano-Metal Particles as Catalyst under Electromagnetic Heating for in-Situ Heavy Oil Recovery. *J. Petrol. Sci. Eng.* **2013,** *112*, 258-265.

(65) Hamedi Shokrlu, Y.; Babadagli, T. In-Situ Upgrading of Heavy Oil/Bitumen During Steam Injection by Use of Metal Nanoparticles: A Study on In-Situ Catalysis and Catalyst Transportation. *SPE Reservoir Eval. Eng.* **2013,** *16*, 333-344.

(66) Wu, C.; Su, J.; Zhang, R.; Lei, G.; Cao, Y. The Use of a Nano-Nickel Catalyst for Upgrading Extra-Heavy Oil by an Aquathermolysis Treatment under Steam Injection Conditions. *Petrol. Sci. Technol.* **2013,** *31*, 2211-2218.

(67) Alkhaldi, S.; Husein, M. M. Hydrocracking of Heavy Oil by Means of in Situ Prepared Ultradispersed Nickel Nanocatalyst. *Energy Fuels* **2014,** *28*, 643-649.

(68) Hamedi Shokrlu, Y.; Babadagli, T. Kinetics of the in-Situ Upgrading of Heavy Oil by Nickel Nanoparticle Catalysts and Its Effect on Cyclic-Steam-Stimulation Recovery Factor. *SPE Reservoir Eval. Eng.* **2014,** *17*, 355-364.

(69) Greff, J.; Babadagli, T., Catalytic Effects of Nano-Size Metal Ions in Breaking Asphaltene Molecules During Thermal Recovery of Heavy-

Oil. In *SPE Annual Technical Conference and Exhibition*, Society of Petroleum Engineers: Denver, Colorado, USA, 2011.

(70) Hendraningrat, L.; Souraki, Y.; Torsater, O., Experimental Investigation of Decalin and Metal Nanoparticles-Assisted Bitumen Upgrading During Catalytic Aquathermolysis. In *SPE/EAGE European Unconventional Conference and Exhibition*, Society of Petroleum Engineers: Vienna, Austria, 2014.

(71) Nassar, N. N.; Husein, M. M. Ultradispersed Particles in Heavy Oil: Part I, Preparation and Stabilization of Iron Oxide/Hydroxide. *Fuel Process. Technol.* **2010,** *91*, 164-168.

(72) Nassar, N. N.; Husein, M. M.; Pereira-Almao, P. Ultradispersed Particles in Heavy Oil: Part II, Sorption of $H_2S(g)$. *Fuel Process. Technol.* **2010,** *91*, 169-174.

(73) Abdrafikova, I. M.; Kayukova, G. P.; Petrov, S. M.; Ramazanova, A. I.; Musin, R. Z.; Morozov, V. I. Conversion of Extra-Heavy Ashal'chinskoe Oil in Hydrothermal Catalytic System. *Petro. Chem.* **2015,** *55*, 104-111.

(74) Ovalles, C.; Rivero, V.; Salazar, A. Downhole Upgrading of Orinoco Basin Extra-Heavy Crude Oil Using Hydrogen Donors under Steam Injection Conditions. Effect of the Presence of Iron Nanocatalysts. *Catalysts* **2015,** *5*, 286-297.

(75) Hamedi Shokrlu, Y.; Babadagli, T., Effects of Nano-Sized Metals on Viscosity Reduction of Heavy Oil/Bitumen During Thermal Applications. In *Canadian Unconventional Resources & International Petroleum Conference*, Society of Petroleum Engineers: Calgary, Alberta, Canada, 2010.

(76) Galarraga, C. E.; Pereira-Almao, P. Hydrocracking of Athabasca Bitumen Using Submicronic Multimetallic Catalysts at near in-Reservoir Conditions. *Energy Fuels* **2010,** *24*, 2383-2389.

(77) Hashemi, R.; Nassar, N. N.; Pereira-Almao, P. Transport Behavior of Multimetallic Ultradispersed Nanoparticles in an Oil-Sands-Packed Bed Column at a High Temperature and Pressure. *Energy Fuels* **2012,** *26*, 1645-1655.

(78) Hashemi, R.; Nassar, N. N.; Pereira Almao, P. Enhanced Heavy Oil Recovery by in Situ Prepared Ultradispersed Multimetallic Nanoparticles: A Study of Hot Fluid Flooding for Athabasca Bitumen Recovery. *Energy Fuels* **2013,** *27*, 2194-2201.

(79) Hashemi, R.; Nassar, N. N.; Pereira Almao, P. In Situ Upgrading of Athabasca Bitumen Using Multimetallic Ultradispersed Nanocatalysts in an Oil Sands Packed-Bed Column: Part 1. Produced Liquid Quality Enhancement. *Energy Fuels* **2014,** *28*, 1338-1350.

(80) Hashemi, R.; Nassar, N. N.; Pereira Almao, P. In Situ Upgrading of Athabasca Bitumen Using Multimetallic Ultradispersed Nanocatalysts in an Oil Sands Packed-Bed Column: Part 2. Solid Analysis and Gaseous Product Distribution. *Energy Fuels* **2014,** *28*, 1351-1361.

(81) Liu, X.; Yang, Z.; Zhao, M.; Li, X.; Su, C.; Zhang, Z. Preparation of Silica-Supported NanoFe/Ni Alloy and Its Application in Viscosity Reduction of Heavy Oil. *Micro Nano Lett.* **2015,** *10*, 167-171.

(82) Li, K.; Hou, B.; Wang, L.; Cui, Y. Application of Carbon Nanocatalysts in Upgrading Heavy Crude Oil Assisted with Microwave Heating. *Nano Lett.* **2014,** *14*, 3002-3008.

(83) Wang, H.; Wu, Y.; He, L.; Liu, Z. Supporting Tungsten Oxide on Zirconia by Hydrothermal and Impregnation Methods and Its Use as a Catalyst to Reduce the Viscosity of Heavy Crude Oil. *Energy Fuels* **2012,** *26*, 6518-6527.

(84) Lai, W.; Chen, Z.; Zhu, J.; Yang, L.; Zheng, J.; Yi, X.; Fang, W. A Nimos Flower-Like Structure with Self-Assembled Nanosheets as High-Performance Hydrodesulfurization Catalysts. *Nanoscale* **2016,** *8*, 3823-3833.

(85) Tang, T.; Zhang, L.; Fu, W.; Ma, Y.; Xu, J.; Jiang, J.; Fang, G.; Xiao, F. S. Design and Synthesis of Metal Sulfide Catalysts Supported on Zeolite Nanofiber Bundles with Unprecedented Hydrodesulfurization Activities. *J. Am. Chem. Soc.* **2013,** *135*, 11437-11440.

(86) Zhao, Q.; Yan, Z.; Chen, C.; Chen, J. Spinels: Controlled Preparation, Oxygen Reduction/Evolution Reaction Application, and Beyond. *Chem. Rev.* **2017,** *117*, 10121-10211.

(87) Shoemaker, D. P.; Li, J.; Seshadri, R. Unraveling Atomic Positions in an Oxide Spinel with Two Jahn-Teller Ions: Local Structure Investigation of $CuMn_2O_4$. *J. Am. Chem. Soc.* **2009,** *131*, 11450-11457.

(88) Yu, L.; Zhang, L.; Wu, H. B.; Lou, X. W. Formation of $Ni_xCo_{3-x}S_4$ Hollow Nanoprisms with Enhanced Pseudocapacitive Properties. *Angew. Chem. Int. Ed.* **2014,** *53*, 3711-3714.

(89) Chauhan, M.; Reddy, K. P.; Gopinath, C. S.; Deka, S. Copper Cobalt Sulfide Nanosheets Realizing a Promising Electrocatalytic Oxygen Evolution Reaction. *ACS Catal.* **2017,** *7*, 5871-5879.

(90) Yan, Y.; Xia, B.; Ge, X.; Liu, Z.; Wang, J. Y.; Wang, X. Ultrathin MoS$_2$ Nanoplates with Rich Active Sites as Highly Efficient Catalyst for Hydrogen Evolution. *ACS Appl. Mater. Interfaces* **2013,** *5,* 12794-12798.

(91) Afanasiev, P.; Xia, G. F.; Berhault, G.; Jouguet, B.; Lacroix, M. Surfactant-Assisted Synthesis of Highly Dispersed Molybdenum Sulfide. *Chem. Mater.* **1999,** *11,* 3216-3219.

(92) Zhao, Y.; Kuai, L.; Liu, Y.; Wang, P.; Arandiyan, H.; Cao, S.; Zhang, J.; Li, F.; Wang, Q.; Geng, B.; Sun, H. Well-Constructed Single-Layer Molybdenum Disulfide Nanorose Cross-Linked by Three Dimensional-Reduced Graphene Oxide Network for Superior Water Splitting and Lithium Storage Property. *Sci. Rep.* **2015,** *5,* 8722.

(93) Wang, P. P.; Sun, H.; Ji, Y.; Li, W.; Wang, X. Three-Dimensional Assembly of Single-Layered MoS$_2$. *Adv. Mater.* **2014,** *26,* 964-969.

(94) Hwang, H.; Kim, H.; Cho, J. MoS$_2$ Nanoplates Consisting of Disordered Graphene-Like Layers for High Rate Lithium Battery Anode Materials. *Nano Letters* **2011,** *11,* 4826-4830.

(95) Miao, J.; Xiao, F. X.; Yang, H. B.; Khoo, S. Y.; Chen, J.; Fan, Z.; Hsu, Y. Y.; Chen, H. M.; Zhang, H.; Liu, B. Hierarchical Ni-Mo-S Nanosheets on Carbon Fiber Cloth: A Flexible Electrode for Efficient Hydrogen Generation in Neutral Electrolyte. *Sci. Adv.* **2015,** *1,* e1500259.

(96) Ho, T. C.; McConnachie, J. M. Ultra-Deep Hydrodesulfurization on MoS$_2$ and Co$_{0.1}$MoS$_2$: Intrinsic vs. Environmental Factors. *J. Catal.* **2011,** *277,* 117-122.

(97) Yi, Y. J.; Zhang, B. S.; Jin, X.; Wang, L.; Williams, C. T.; Xiong, G.; Su, D. S.; Liang, C. H. Unsupported NiMoW Sulfide Catalysts for Hydrodesulfurization of Dibenzothiophene by Thermal Decomposition of Thiosalts. *J. Mol. Catal. A-Chem.* **2011,** *351,* 120-127.

(98) Yoosuk, B.; Kim, J. H.; Song, C.; Ngamcharussrivichai, C.; Prasassarakich, P. Highly Active MoS$_2$, CoMoS$_2$ and NiMoS$_2$ Unsupported Catalysts Prepared by Hydrothermal Synthesis for Hydrodesulfurization of 4,6-Dimethyldibenzothiophene. *Catal. Today* **2008,** *130,* 14-23.

(99) Yoosuk, B.; Song, C. S.; Kim, J. H.; Ngamcharussrivichai, C.; Prasassarakich, P. Effects of Preparation Conditions in Hydrothermal Synthesis of Highly Active Unsupported NiMo Sulfide Catalysts for

Simultaneous Hydrodesulfurization of Dibenzothiophene and 4,6-Dimethyldibenzothiophene. *Catal. Today* **2010,** *149*, 52-61.

(100) Guo, K.; Hansen, V. F.; Li, H. L.; Yu, Z. X. Monodispersed Nickel and Cobalt Nanoparticles in Desulfurization of Thiophene for in-Situ Upgrading of Heavy Crude Oil. *Fuel* **2018,** *211*, 697-703.

(101) Guo, K.; Gu, M. F.; Yu, Z. X. Carbon Nanocatalysts for Aquathermolysis of Heavy Crude Oil: Insights into Thiophene Hydrodesulfurization. *Energy Technol.* **2017,** *5*, 1228-1234.

(102) Guo, K.; Zhang, Y. H.; Shi, Q.; Yu, Z. X. The Effect of Carbon-Supported Nickel Nanoparticles in the Reduction of Carboxylic Acids for in Situ Upgrading of Heavy Crude Oil. *Energy Fuels* **2017,** *31*, 6045-6055.

(103) Shah, A. A.; Fishwick, R. P.; Leeke, G. A.; Wood, J.; Rigby, S. P.; Greaves, M. Experimental Optimization of Catalytic Process in Situ for Heavy-Oil and Bitumen Upgrading. *J. Can. Petrol. Technol.* **2013,** *50*, 33-47.

(104) Montgomery, W.; Court, R. W.; Rees, A. C.; Sephton, M. A. High Temperature Reactions of Water with Heavy Oil and Bitumen: Insights into Aquathermolysis Chemistry During Steam-Assisted Recovery. *Fuel* **2013,** *113*, 426-434.

(105) Li, D.; Gong, Y.; Pan, C. Facile Synthesis of Hybrid CNTs/NiCo$_2$S$_4$ Composite for High Performance Supercapacitors. *Scientific Reports* **2016,** *6*, 29788.

(106) Shen, L. F.; Wang, J.; Xu, G. Y.; Li, H. S.; Dou, H.; Zhang, X. G. NiCo$_2$S$_4$ Nanosheets Grown on Nitrogen-Doped Carbon Foams as an Advanced Electrode for Supercapacitors. *Adv. Energy Mater.* **2015,** *5*, 1400977.

# Appendices

## *Appendix A  Paper I*

# Paper I

### *In-situ* heavy and extra-heavy oil recovery: A review

**Kun Guo**, Hailong Li, and Zhixin Yu

## *Appendix B    Paper II*

# Paper II

## Metallic nanoparticles for enhanced heavy oil recovery: promises and challenges

**Kun Guo**, Hailong Li, and Zhixin Yu

### Appendix C   Paper III and Supporting Information

# Paper III

## Monodispersed nickel and cobalt nanoparticles in desulfurization of thiophene for in-situ upgrading of heavy crude oil

**Kun Guo**, Vidar Folke Hansen, Hailong Li, and Zhixin Yu

## Appendix D    Paper IV and Supporting Information

# Paper IV

**Carbon nanocatalysts for aquathermolysis of heavy crude oil: insights into thiophene hydrodesulfurization**

**Kun Guo**, Minfen Gu, and Zhixin Yu

# Paper V

### The effect of carbon-supported nickel nanoparticles in the reduction of carboxylic acids for in situ upgrading of heavy crude oil

**Kun Guo**, Yahe Zhang, Quan Shi, and Zhixin Yu

## *Appendix F    Paper VI and Supporting Information*

# Paper VI

## Nickel cobalt thiospinel nanoparticles as hydrodesulfurization catalysts: the importance of cation position, structural stability and sulfur vacancy

**Kun Guo**, Yi Ding, Jun Luo and Zhixin Yu

Submitted.

***Appendix G   Paper VII and Supporting Information***

# Paper VII

**One-step synthesis of ultrafine MoNiS and MoCoS monolayers as high-performance catalysts for hydrodesulfurization and hydrodenitrogenation**

**Kun Guo**, Yi Ding, and Zhixin Yu

Submitted.